From PET detectors to PET scanners

John L. Humm[1], Anatoly Rosenfeld[2], Alberto Del Guerra[3]

[1] Department of Medical Physics, Memorial Sloan Kettering Cancer Center, New York, USA
[2] Physics Department, University of Wollongong, New South Wales, Australia
[3] Department of Physics “E. Fermi”, University of Pisa, Pisa, Italy

Abstract. This review describes the properties of available and emerging radiation detector and read-out technologies and discusses how they may affect PET scanner performance. After a general introduction, there is a section in which the physical properties of several different detector scintillators are compared. This is followed by a discussion of recent advances in read-out electronics. Finally, the physical performance of the several commercial PET scanners is summarized.

Keywords: Positron emission tomography – PET detectors – BGO – LSO – Depth of interaction

Eur J Nucl Med Mol Imaging (2003) 30:1574–1597
DOI 10.1007/s00259-003-1266-2

Introduction

Clinical needs and advantages of PET in modern diagnosis

The recent explosion of interest in positron emission tomography (PET) imaging can be attributed to two recent events:

1. Reimbursement for FDG PET scanning in oncology
2. Evidence that PET will be a key modality to interrogate cancer and cardiac biology, and will serve as a critical component of “molecular imaging,” a technology that will permit individualized therapy of disease.

The current generation of dedicated PET scanners tend to use BGO (bismuth germinate) detectors, while hybrid PET/SPET systems use NaI:Tl (sodium iodide, thallium activated) detector based gamma cameras with dedicated high count rate electronics and coincidence detection. Recently, commercial clinical PET scanners have become available which use alternative crystal technologies, e.g., GSO (germanium oxyorthosilicate) or LSO (lutetium oxyorthosilicate). Each company explains the advantages of their crystal technology, providing a bewildering assortment of facts and leaving the potential buyer of a PET camera frequently wondering how the detectors impact upon the quality of clinical images, patient throughput, etc. The objectives of this review are: (a) to provide the reader with an overview of the physics of PET, (b) to inform the reader about the properties of the various crystal detectors, (c) to describe the implications of these crystal properties for scanner performance, something that is difficult to discuss for commercial systems in isolation because of other significant factors in camera design, e.g., 2D vs. 3D, scanner field of view, intrinsic spatial and energy resolution, etc., (d) to discuss new crystals, which are being evaluated for experimental PET scanners with potential applications on future clinical units, (e) to discuss developments associated with detector configurations and read-out technology that may improve scanner performance, such as “depth of interaction” techniques, and (f) to discuss the dedicated scanners for high-resolution small animal imaging, PET mammography and radiotherapy PET simulation.

Principles of PET operation

Since the construction of the first scanner, it has been recognized that PET is a powerful and sensitive technique for functional imaging in the field of nuclear medicine [1, 2, 3, 4, 5]. Once the pharmaceutical is injected into the patient, the distribution of the tracer can be quantitatively determined within the body (or tumor) from the PET image dataset. This PET image is created when the isotropically emitted positron slows down and annihilates with electrons in tissue producing two back-to-back 511-keV photons, which are measured in elec-

John L. Humm (✉)
Department of Medical Physics,
Memorial Sloan Kettering Cancer Center, 1275 York Avenue,
New York, NY 10021 USA
e-mail: hummj@mskcc.org
Tel.: +1-212-6397367

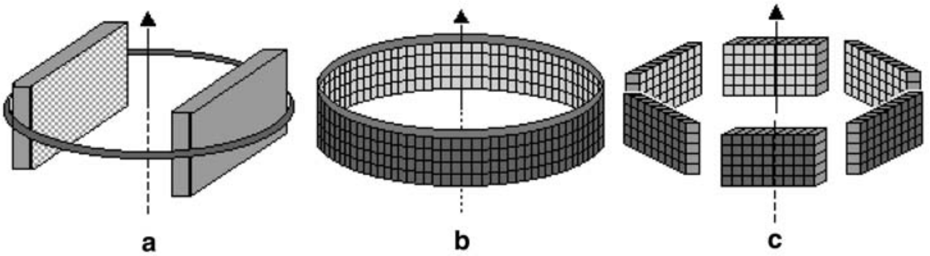

Fig. 1a–c. Examples of PET systems: detectors mounted on a rotating gantry (**a**), or circular (**b**) or polygonal detector rings (**c**). Commercial cameras generally offer a multiring geometry, with tens of thousands of scintillation elements

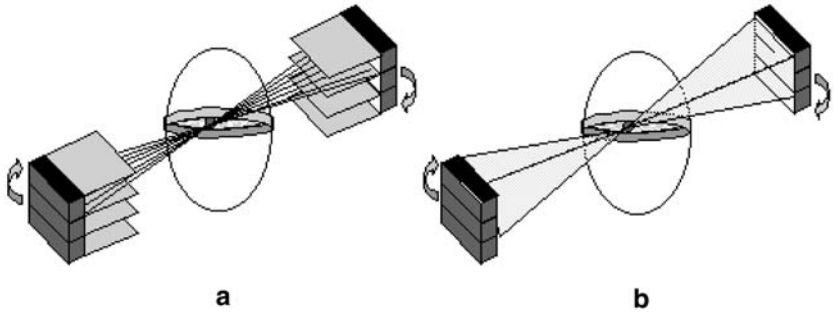

Fig. 2a, b. "PET acquisition" schemes: **a** 2D inter-ring septa allow separation of slices; **b** 3D without septa, with an increase in the sensitivity

tronic coincidence by using opposing pairs of detectors. Each registered coincident 511-keV pair is referred to as an event. The electronic coincidence detection intrinsically implies alignment, so antiscattering and passive collimators are not needed. For this reason, PET exhibits higher detection efficiency relative to single-photon emission tomography (SPET). Several configurations of detectors have been used in commercial PET cameras. These include (a) detectors mounted on a rotating gantry or in a stationary configuration (Fig. 1a), (b) detectors arranged in a circular ring (Fig. 1b), or (c) detectors arranged in a polygonal ring (Fig. 1c), to provide intrinsic tomographic image sets.

PET scanners can be designed to operate in 2D or 3D mode, or as 3D-only systems. In 2D mode, the collection of the emission radiation is restricted to each individual slice (or adjacent slices), by using septa (Fig. 2a). This reduces the contributions from scatter and random coincidences to the acquired emission data, with a consequent reduction in the overall sensitivity. In 3D mode, tomographs recover the isotropic properties of radiation emission. The acquisition is no longer limited to a planar slice, but is performed on the whole solid angle between any detector pair, therefore achieving a fully 3D image (Fig. 2b). The removal of the inter-ring septal shield results in a substantial increase in the sensitivity, at the expense of an increased scatter fraction and count rate performance at high patient administered activities.

Photon interactions with matter and the role of each mechanism for PET

Positrons are emitted with a kinetic energy greater than zero, and are slowed down through multiple Coulomb interactions in biological tissue. Energy loss continues until the positron reaches thermal equilibrium with the surrounding medium, when annihilation with an electron occurs [6, 7].

The range of the positron depends on the electron density of the medium. In water, which is the major component of biological tissue, the range of the positrons emitted from PET radionuclides is about 1–2 mm, as reported in Table 1 [2, 8]. An ideal tomograph should accurately measure the activity distribution in the body, i.e., the positron emission points. Actually, a tomograph can only detect the annihilation point: the range of the positron separates these two points. This *range effect* degrades the spatial resolution, introducing a blurring in the image. The contribution of this effect to the total spatial resolution is reported in Table 1 for several isotopes [3].

In general, the annihilation occurs when the positron has reached thermal equilibrium with an electron not at rest. In fact, electrons constitute a statistical system of particles (Fermi gas) with an isotropic distribution of momentum in space. An approximated calculation of the deviation from the co-linearity of the emitted photons can be made by just considering the thermal motion of the particles and the conservation of the Fermi momentum [9, 10, 11]. This gives 180°±0.25°.[1] The distribution of the angular deviation in water (e.g., biological tissue) is assumed to be Gaussian with FWHM ≈0.5°. The con-

---

[1] This result is lower than the experimental one [12, 13]. The differences are due to the formation of a particle with higher momentum, the *positronium*, a hydrogenoid atom where the positron is in a bound system with an electron. The positronium annihilates in 2γ either from the *para-positronium* (single state) or predominantly from the *ortho-positronium* (triplet state).

Table 1. Numerical data for the radioisotopes most commonly used in PET. Electrons and positrons do not move along a straight line in matter because of the high number of interactions with small energy exchange; therefore their path length is always longer than their range

Isotope	Half-life (min)	Average kinetic energy (Mev)	Maximum kinetic energy (MeV)	Average range in water (mm)	Path length (mm)	FWHM (mm)	FWTM (mm)[a]
^{11}C	20.4	0.385	0.960	1.7	4.1	0.28	1.86
^{13}N	10.0	0.491	1.198	2.0	5.1		
^{15}O	2.0	0.735	1.732	2.7	7.3		
^{18}F	109.8	0.242	0.633	1.4	2.4	0.22	1.09
^{68}Ga	68.3	0.783	1.880	1.7		1.35	5.92
^{82}Rb	1.3	1.32	4.39			2.60	13.20

[a] Together with the full-width at half-maximum (FWHM), the full-width at tenth-maximum (FWTM) is also given to estimate the deviation of the range distribution from a Gaussian. In a Gaussian distribution the relation between FWHM and FWTM is FWTM=1.82×FWHM

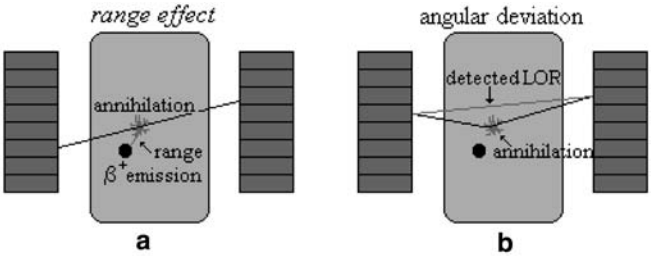

Fig. 3a, b. Fundamental limits in PET. **a** *Range effect*: the detected line of response (LOR) contains the annihilation point, not the emission point. **b** 2 γ non-co-linearity: the tomograph measures an LOR on which the annihilation point does not lie

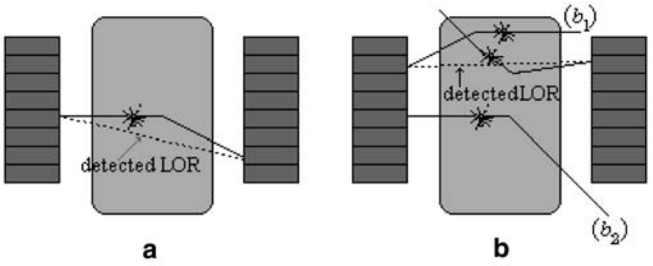

Fig. 4a, b. Effects of Compton scatter in the field of view. **a** An incorrect LOR is recorded. **b** The detected LOR is given by two photons emerging from different annihilation points (**b$_1$**), or the coincidence is lost (**b$_2$**). The symbol * indicates the annihilation point

tribution to the spatial distribution in the center of a detector ring of diameter D can be parameterized as:

$$\mathrm{FWHM} \approx \Delta\theta \times D/4 = 0.0022 \times D$$

with both FWHM and D measured in meters. By setting $\Delta\theta$ to a value of 0.5° (8.7 mrad), this means a contribution to the spatial resolution of 2.2 mm FWHM per meter of detector separation.

The *range effect* and the *2 γ non-co-linearity*, as described above, are fundamental physical resolution limits in PET (Fig. 3). Their effects degrade the spatial resolution, causing a blurring in the reconstructed image. This is especially evident for isotopes with a high E_{max} (i.e., a long positron range) and for whole-body PET systems, where the detector separation is greater than on dedicated brain or animal scanners.

The two 511-keV annihilation photons have a "*mean free path*" of about 10.4 cm in water. The human head and chest have dimensions of the order of 20 cm. This means that in whole-body PET, approximately only 15% of photon pairs have no interaction within the biological tissue. In most cases, one or both photons will be either absorbed or Compton scattered. Absorption of gamma rays diminishes the number of detected photons. Although reducing photon statistics, an attenuation correction can be performed to obtain quantitative information. On the other hand, Compton scattering of the photons in tissue results in inaccurate *line of response* (LOR) counting, as shown in Fig. 4, generating noise in the reconstructed image. While the range effect and the angular deviation are intrinsic physical limits, attenuation and scattering decrease the image quality by reducing count statistics and degrading image contrast. Loss of emission counts through attenuation can be corrected by measuring the transmission profile through the patient with a coincidence source, e.g., ^{68}Ge, a singles source, e.g., ^{137}Cs, or a CT scanner.

Whereas accurate attenuation correction can be performed using a transmission scan by any of the three means cited above, correction for scatter within the patient is considerably more difficult. In 2D, the scatter fraction, i.e., the ratio of scattered to total recorded events, is approximately 10% and does not greatly depend upon the size of the patient being scanned. In 3D, the scatter fraction is already 30–40% within the head, and can be significantly higher in the pelvis. Scatter is most effectively eliminated by energy discrimination, but the energy resolution of scintillators used for PET, in particular BGO, limits the use of narrow energy windows. PET scan protocols usually strive for increased sensitivity, accomplished at the expense of energy resolution. Fortunately, Compton scatter of 511-keV photons is generally narrow angle. Acquisition windows generally have a threshold of about 350 keV to accept small-angle Compton scatter. Several algorithmic methods model the emission and correct for scatter. The reader is referred to the review by Zaidi [14] of the different scatter correction methods.

Scintillators

Energy deposition within the scintillator

Inorganic scintillator crystals are the most commonly used detectors for PET. Annihilation photons interact within the scintillator through Rayleigh, Compton, and photoelectric effects. Only the latter two release energy to the detector, making the photons "detectable." Rayleigh scattering can be ignored at typical PET energies. The annihilation photon could deposit a fraction or all of its energy within the crystal. The deposition can occur in one location by photoelectric effect[2], or at several points within the same crystal by successive Compton interactions, or in different (usually adjacent) crystals in a pixellated matrix.

The absorbed energy causes the crystal lattice to make a transition to a higher energy state, from which it may undergo decay after a characteristic time by emitting lower energy photons, the "*scintillation photons*" that are detected by the photocathode of a photomultiplier tube. Self-absorption of the scintillation photons by the scintillator must be minimal, i.e., the attenuation length must be much longer than the crystal thickness. The amplitude of the electronic signal produced is proportional to the number of scintillation photons, and thus to the energy deposited within the crystal. Energy thresholding can then allow the rejection of a large fraction of events scattered within the patient, which have sufficiently low energy to fall below the energy discrimination window.

Photoelectric and Compton cross-sections are a function of the density (ρ) and of the effective atomic number (Z_{eff}) of the crystal. The atomic cross-section for photoelectric effect is proportional to $\rho \cdot Z_{\mathrm{eff}}^{n} / E_{\gamma}^{m}$, where n and m are both function of the energy: n is about 4 at 100 keV and gradually rises to 4.6 at 3 MeV, whereas m decreases slowly from 3 at 100 keV to 1 at 5 MeV. The cross-section for Compton scattering is proportional to $\rho \cdot Z_{\mathrm{eff}}/A$, where A is the mass number. Z_{eff}/A is almost constant, at 0.45±0.05, for all elements except hydrogen. A high density favors the interaction of the photon in the crystal, whilst a higher Z_{eff} value increases the number of photoelectric (total absorption) occurrences with respect to Compton scattering. Therefore, high Z_{eff} crystals are to be preferred. In fact, if a photon, scattered within the patient, is absorbed via photoelectric effect, this event can be rejected with energy discrimination. Compton events in the crystal may reduce the effectiveness of this discrimination.

The decay time and the light yield are important physical properties of the crystal. The first is the most important parameter to select the temporal coincidence window: a long decay time needs a longer coincidence timing window, and therefore results in a higher yield of random coincidences per unit activity. The scintillation photon wavelength has to match the properties of the photocathode. A greater light yield (number of photons per MeV) in the photoemission zone implies a more linear response, a better energy resolution, and a more accurate spatial resolution. This is particularly relevant for the new position-sensitive phototubes, which work by weighing the energy depositions within the crystal. Unfortunately, fast emission is often coupled to a low light yield, and vice versa.

Scintillator materials

The 511-keV photon attenuation coefficient for the scintillation detector is the main parameter which determines detector sensitivity. Light output of the scintillator determines detector energy resolution. The lifetime of the fluorescent transition affects the count rate performance of the detector. These are the three most important physical attributes affecting PET detector performance. The basic component of a PET detector is a block of scintillator material. This scintillator is responsible for the conversion of ionizing energy deposited from 511-keV photons to light, which is then detected and amplified by the photodetector. Scintillator materials can be organic, plastic, liquid, or inorganic.[3] Plastic scintillators are useful for tissue (water)-equivalent dosimetry in electron and gamma ray fields since the energy deposited by ionizing radiation will be similar to tissue or water. Liquid scintillators are useful for measurements involving radioactive gases, for example tritium, important for environment monitoring near power plants. For all current commercial PET scanners, inorganic scintillators are used.

---

[2] For ultra-high-resolution PET scanner, the fluorescent photon should also be considered.

[3] Webpages of manufacturers of scintillation materials: 1, http://www.bicron.com; 2, http://www.rexon.com; 3, http://www.crystran.co.uk; 4, http://www.hilger-crystals.co.uk; 5, http://www.scionixusa.com/scintillation_detectors.html; 6, http://www.utari.com; 7, http://www.girmet.ru/~ramet/scintillator.htm; 8, an exceptionally rich source of up-to-date reference material on scintillators is the Web Page, University of California, Lawrence Berkeley National Laboratories, Center for Functional Imaging, http://cfi.lbl.gov/instrumentation/Publications.html.

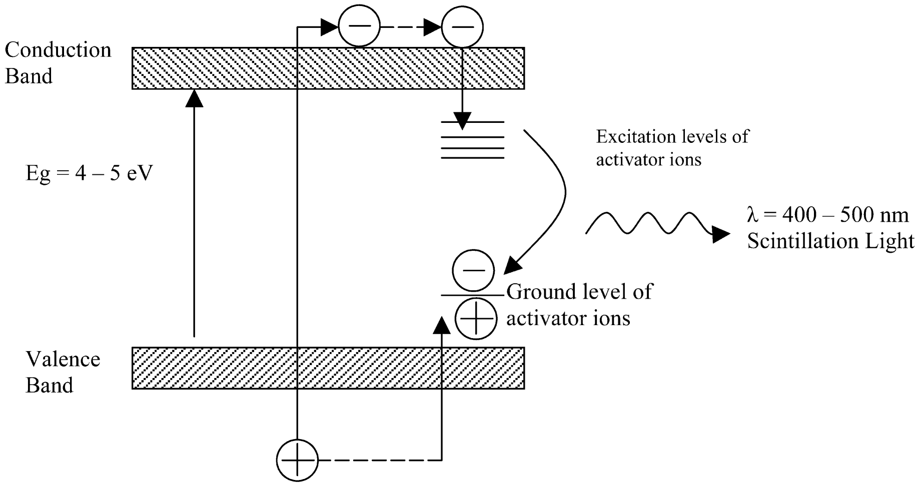

Fig. 5. The band structure of an inorganic scintillator

Inorganic scintillators

Inorganic scintillators are usually a single ionic crystal in which the valence and conduction bands are separated by a 4- to 6-eV forbidden energy gap. The band structure explaining simplified operation of the scintillator is shown in Fig. 5. Ionizing radiation, upon interaction with the crystal, causes electrons to jump from the valence band to the conducting band. This creates an electron-hole (e-h) pair. Whereas electrons in the conduction are still bound to the crystal, they are no longer bound to an individual atom, and therefore can move freely through the crystal lattice. The average energy to produce an electron-hole pair is much greater than the 5-eV width of the forbidden gap E_g, usually about three times greater. This is because part of the energy transferred to the crystal is transferred in the form of phonon energy, i.e., quantized collective mechanical oscillations within the crystal.

Inorganic scintillators are of two types. *Activated scintillators* such as NaI:Tl or Lu_2SiO_5:Ce become fluorescent through the introduction of a small amount of impurity dopant into the pure single host crystal. The second type is *self-activated scintillators* such as $Bi_4Ge_3O_{12}$ (or just BGO), where the activator atoms are a major constituent of the crystal. The role of the activator is to produce quantum energy levels (ground and excited states) within the forbidden gap. The electron and hole are transferred non-radiatively to the ionised dopant (activator) during migration in the crystal, creating their own activator-excited states (Fig. 5). Relaxation of an electron trapped from an excitation level of the activation center to the ground state results in the emission of a light quantum or scintillation photon. The electrons captured within these excited activator states emit scintillating spectra with a maximum emission intensity corresponding to wavelength $\lambda_{m.}$

The efficiency of this conversion process [15], i.e., number of photons emitted by the scintillator, can be presented as:

$$N_{ph} = \alpha SQ$$

where α is a number of e-h pairs produced in the conduction and valence bands respectively due to the absorption of radiation in the crystal, S is a transport efficiency of e-h pairs to the luminescent center (activator ion), and Q is the quantum efficiency for the luminescent center (probability of a radiative transition to the ground state). Q is not unity because other competitive non-radiative processes can convert the energy to elastic vibrations, e.g., phonons, through the Frank-Condon principle. De-excitation of captured electron and holes, which result in radiationless transitions, is called “quenching.” This mechanism is determined by many factors such as other impurity atom dopants, structural defects during crystal growth, etc. Electrons can create excited configurations with the activator, such that additional energy must be provided before fluorescence photon emission occurs. Such excited non-radiative configurations can be quite long relative to the time required for radiative luminescence, de-excitation only occurring once the activation center absorbs sufficient phonon energy. This process can result in a long photon emission tail “afterglow.” The various factors influencing the efficiency of conversion of absorbed energy to luminescent light intensity can be found in the following references: [16, 17].

Requirements for scintillators in PET scanners

The following characteristics of scintillators are the most important for PET application: attenuation length, detection efficiency, photoelectric fraction, density, luminosity, decay time, energy resolution, emission wavelength, refractive index, mechanical and hydroscopic properties, radiation hardness, cost, and availability on market.

For high intrinsic efficiency, scintillator materials should have both a high effective atomic number Z_{eff} and high density. The important parameter determining the scintillator material's ability to stop 511-keV photons is $\rho Z_{\mathrm{eff}}^{4}$.

The energy (and spatial) resolution is associated with the light yield from the scintillator. The magnitude of the fluorescent light yield will reduce the statistical spread as $(N_{\mathrm{ph}})^{-1/2}$. In most scintillators the light yield depends on the energy released per electron. The intrinsic energy resolution of a crystal is determined by the degree of statistical spread in the collected number of fluorescent photons for a full 511-keV absorption event within the detector crystal. Several factors affect the intrinsic energy resolution, including inhomogeneity of the activation centers within the crystal, non-uniformity of luminosity of the scintillator crystal as well as unknown causes of the non-proportional response of the scintillator (observed, for example, between different batches of LSO, GSO, LGSO and YSO by Balcerzyk et al. [18]).

For high count rate applications the decay time should be as short as possible to permit good coincidence timing resolution so as to minimize random coincident events. The parameter influencing this is the number of photons emitted per nanosecond. The main contribution to the observed FWHM of time spread can be presented as $\Delta t = \tau / N_{\mathrm{ph}}$ [18], where τ is a decay constant of scintillator and N_{ph} is a total number of photons emitted by the scintillator. According to this expression it is possible to obtain good coincidence resolution for scintillators with moderate light yield but shorter decay constant.

To collect as many light quanta as possible, each crystal is enclosed in a reflective light tight case at all surfaces except at the entrance window of the photodetector. Not all of the emitted fluorescence photons reach the light collection system of the photodetector. There are absorptive losses in the crystal due to the partial overlap of the emission and absorption bands of the crystal. For this reason, crystalline detector materials are selected (or appropriately doped) such that fluorescent emission minimally overlaps with the absorption bands of the crystal, ensuring minimal attenuation losses in thick 30-mm detectors necessary to fully stop 511-keV photons. Secondly, there are losses at the non-perfect reflective surfaces of the detector, with further losses of light quanta at the coupling between the crystal and the photodetector. The actual amount of absorption losses within the crystal is a few percent.

The emission wavelength of the scintillator light should match the light response characteristic of the photodetectors/photocathode. The most useful scintillators for PET applications should have maximum scintillation intensity in the wavelength range 380–440 nm, to match with bi-alkali photomultiplier tubes (PMTs), which have maximum sensitivity in the range 390–410 nm. These losses occur as a result of optical refraction at the interface between the detector and the window of the PMT. This window, usually glass, acts as a seal to maintain a vacuum within the PMT. The photocathode is a thin layer of semiconductor deposited on its inner surface. It is important that the indices of refraction between the detector and PMT window are matched, in order that minimal refraction occurs and almost all of the light quanta incident on the window will be transmitted and reach the photocathode. Refraction causes light quanta to be lost or reflected back into the detector for angles of incidence greater than the critical angle φ_c given by Snell's law $\varphi_c = \sin^{-1}(n_1/n_0)$. Since the index of refraction of typical glass window is 1.5, scintillators with a lower refraction index give a better coupling. Such matching is more closely achieved with some detector materials, e.g., GSO (n=1.85), than others, e.g., BGO (n=2.15).

Once the photon impinges on the photocathode, the optical energy is converted into electron kinetic energy by the photoemission process. The yield of photoelectrons is dependent upon the wavelength of the light emitted by the detector. Since photon energy is inversely proportional to wavelength (Plank's law), shorter wavelength quanta generate a higher yield of photoelectrons. For a photoelectron to be produced, the light quantum must exceed the work function (minimum energy level needed to expel an electron from the surface of the material) of the photocathode. Ideally, one would like to collect each photon emitted by the detector and convert it into a photoelectron at the photocathode. The actual ratio for common commercially available PMTs is 0.2–0.3. This magnitude is referred to as the *quantum efficiency* of the photocathode. It is defined in terms of the number of photo-emitted electrons released by the photocathode per incident light photon. For this reason, a single charge carrier (electron-hole pair) results from an average of about 100 eV expended in the crystal, because of the various energy losses prior to the production of that pair. Such losses include the probability of a light quantum producing a photoelectron, the number of electrons that escape the photocathode, including geometrical losses, in that $<2\pi$ photoelectrons enter the amplification stage of the PMT, etc. Contrast this 100 eV per charge carrier with the corresponding values of 30 eV for a gaseous detector and 3 eV for a solid state detector, where the charge carriers are an electron/positive ion pair and an electron-hole pair respectively.

An alternative to the PMT is silicon photodiodes, which do not require high voltage and have four times better quantum efficiency than the PMT [19, 20]. The maximum spectral sensitivity of Si photodiodes is shifted to the longer wavelength 600–800 nm. New high Z and high-density scintillators with infrared light emission will be advantageous for better matching with silicon photodiodes and increasing the signal to noise (S/N) ratio.

Radiation hardness of scintillators is a further important physical property to avoid production of color centers due to possible radiation defects. These centers can absorb scintillation light and thereby reduce the luminosity of the scintillator.

Table 2. Physical properties of scintillator materials commonly used for PET

Scintillator material	Composition	Density (g/cm^3)	Z_{eff}	Attenuation length for 511-keV gammas (mm)	Probability of PE (%)	Light output (ph/MeV)	Decay time (ns)	Scint. emission wave-length (nm)	Hygroscopic	Refractive index
BGO	$Bi_4Ge_3O_{12}$	7.1	75	10.4	40	9,000	300	480	No	2.15
LSO	Lu_2SiO_5:Ce	7.4	66	11.4	32	30,000	40	420	No	1.82
NaI:Tl	NaI:Tl	3.67	51	29.1	17	41,000	230	410	Yes	1.85
CsI:Tl	CsI:Tl	4.51	52	22.9	21	66,000	900	550	Slightly	1.80
GSO	Gd_2SiO_5:Ce	6.7	59	14.1	25	8,000	60	440	No	1.85
LGSO	$Lu_{1.8}O_2SiO_3$:Ce					23,000	40	420	No	
LuAP	$LuAlO_3$:Ce	8.3	64.9	10.5	30	12,000	18	365	No	1.94
YAP	$YAlO_3$:Ce	5.5	33.5	21.3	4.2	17,000	30	350	No	1.95
LPS	$Lu_2Si_2O_7$:Ce	6.2	63.8	14.1	29	30,000	30	380	No	
LuAG	$Lu_3Al_5O_{12}$:Ce	6.7	62.9	13.4	27	5,606		510	No	

PE, Photoelectric effect

Characteristics of typical scintillators for PET application

Scintillator materials most suitable for PET scanners are those that satisfy most of the above-mentioned requirements. At the current time these are $Bi_4Ge_3O_{12}$ (BGO), NaI:Tl, Lu_2SiO_5:Ce (LSO), Gd_2SiO_5:Ce (GSO), $Lu_{1.8}O_2SiO_3$:Ce (LGSO), $LuAlO_3$:Ce (LuAP), $YAlO_3$:Ce (YAP), $Lu_2Si_2O_7$:Ce (LPS), $Lu_3Al_5O_{12}$:Ce (LuAG) and CsI:Tl or CsI:Na. A summary of the characteristics of these scintillators is presented in the Table 2. Selection of a specific detector material is based on requirements and specifications of the scanner, as well as the availability of the scintillator material. The cost of manufacturing the detector material is a large contribution to the expense of a PET scanner, and here it depends upon whether it will be a whole-body scanner or a dedicated small animal imaging unit, where both high spatial resolution sensitivity may be the important requirements.

Bismuth germanate ($Bi_4Ge_3O_{12}$) or BGO is a relatively hard, rugged, non-hygroscopic crystal, which does not require hermetic sealing. BGO is a pure inorganic scintillator that requires no activator. The large atomic number of Bi (Z=83) and high density (7.1 g/cm^3) make it the detector material with the greatest attenuation coefficient for 511-keV gamma rays. For example, the photoelectric cross-section at 511 keV for BGO is 60% higher than that for LSO and 2.7 and 5.8 times higher than those for GSO and NaI:Tl respectively. This property is important for the improvement of spatial resolution when the size of separate pixels is large, as in classical light-sharing PET detector modules [21]. The mean path length of a 511-keV photon is 1.1 cm (40% photoelectric fraction), meaning that a 30-mm-thick crystal is almost 3 attenuation lengths. The luminescence comes from the optical transition of the Bi^{3+} ion states within the crystal. The large shift between the optical absorption and the emission spectra of the Bi^{3+} states results in minimal self-absorption, so that the crystal is transparent to its own emission. As a result of this transparency, a small amount of BGO is required to absorb rays allowing thin detector shielding. This enables an array of detectors to be constructed in a closely packed fashion.

The disadvantages of BGO, relative to other detector materials, include its low light yield, ≈20% relative to NaI:Tl, as a result of which it exhibits an inferior energy resolution at 511 keV of only 18% compared to 8% for NaI:Tl. Also, since the emission is partly in the region above 500 nm, where PMTs are less sensitive, the relative yield of standard photocathodes compared to NaI:Tl is only ~10–15%. Also the timing properties (τ=300 ns) contribute to a further reduction in the energy resolution of BGO detectors. For scintillators with slow fluorescent emission characteristics, there is always a trade-off between energy and timing resolution. Reducing the pulse integration time improves the time resolution (and consequently the count rate performance), but results in a decrease in the amplitude of the signal, thereby reducing the energy resolution. The decay time of BGO is about 300 ns at room temperature, and is comparable to that of NaI:Tl. However, the afterglow is much lower, typically about 0.005% after 3 ms. Another disadvantage of BGO is that the fluorescence intensity increases by 1% per 1°C decrease in temperature, necessitating more stringent environmental regulation of BGO scanners relative to some of the other detector materials. Nevertheless, these properties combined with the widespread availability of BGO have rendered it the most widely used scintillator for commercial PET scanners.

NaI:Tl is a scintillator material with highest luminosity, and the scintillator of choice for imaging with gamma cameras, some of which have coincidence detection options. However, for 511-keV PET imaging, both the Z_{eff} and the density are suboptimal relative to BGO and other scintillators. One great advantage of NaI:Tl is the ability to produce large ingots with a diameter of about 80 cm and the cheaper manufacturing costs relative to other scintillator materials. The recent development of curved NaI:Tl crystals has found application in new high-resolution PET scanners [22] (C-PET, ADAC-Phillips, Milpitas, CA), replacing the six flat panel hexagonal PET ring design of the PENNPET [23]. One big advantage of NaI:Tl is the high light output, which allows energy resolutions of the order of 8% at 511 keV. However, NaI:Tl is hygroscopic, which requires that the crystals be hermetically sealed, usually in a thin aluminum container, to prevent the entrance of moisture. Moisture causes the crystal to develop yellow spots, which causes uneven light transmission.

Lutetium oxyorthosilicate (Lu_2SiO_5) or LSO is one of the most suitable scintillator materials for PET. It has the second highest $\rho Z_{eff}{}^4$, the parameter determining detector sensitivity. Since one must register both coincident photons to register an event, this factor appears in quadrature when comparing different scintillation detector materials. Nevertheless, LSO exhibits only a 1.5 times lower sensitivity than BGO for the detection of coincident 511-keV gamma rays. The high light yield (30,000 photons/MeV), short time decay of ≈40 ns, and relatively high and good mechanical properties all make LSO a highly suitable crystal for commercial PET scanner application [15]. In 3D PET scanners, where count rate performance is extremely important, the advantage of LSO is the ability to reduce the coincidence timing window from 12 to 6 ns (CTI Reveal). LSO is an activated scintillator, in which Ce^{+3} ions are used as the activator. The effective luminescent center resulting from the cerium activator emits light with a mean wavelength of about 420 nm. Detailed investigations of LSO produced by different manufacturers in the USA, Russia, and Japan demonstrated that an energy resolution of 7.3% was attainable upon exposure to a 662-keV test source of ^{137}Cs [24]. The timing resolution for $3 \times 3 \times 20$ mm^3 LSO crystals was about 450 ps using an avalanche photodiode [24]. This excellent time resolution is chiefly due to the absence of longer time components in the light decay, such as occurs with NaI:Tl, CsI:Tl, and BGO. This advantage of LSO may allow its use in the design of time of flight PET scanners. Disadvantages observed in this material are the purported non-proportionality of light output to the deposited energy, and possible different decay times in samples obtained from larger and different ingots [25,26]. Energy resolutions vary between samples and exhibit a high dependence upon the photon energy. For example, the energy resolution shows an $E^{-1/2}$ type dependence with photon energy, i.e., ≈5% for ^{60}Co gamma rays, reducing to 40% for the 140-keV photons of ^{99m}Tc. For more details on the variability between samples, refer to Balcerzyk et al. [27]. This variability of Ce activator concentration between LSO samples limits the energy resolution of current clinical LSO scanners, although greatly superior to BGO. The solid state properties are still being investigated with this scintillator, with the hope of achieving a more controlled and reproducible light output. The variation in the light output per unit time between crystals could be constructively used in PET modules for depth of interaction identification, to improve the spatial resolution of events far from the axis of the scanner (discussed in a later section). Another disadvantage of LSO is the presence of a naturally long-lived isotope of lutetium (^{176}Lu) within the crystal. It has been estimated that 2.6% of the lutetium in LSO is ^{176}Lu, which has a half-life of approximately 4×10^{10} years, and gives rise to two prompt gamma rays of 201 and 306 keV (sum peak 507 keV) with an 88% yield, leading to a measured background count rate of 240 cps/cc of LSO crystal [28]. In a clinical scanner such as the CTI Reveal, this translates into singles and trues count rates of 100,000 cps and 10,000 cps respectively. Whereas these levels have a negligible impact on conventional clinical emission scans, they may impact on dedicated small animal PET in research studies with low count rates, and would significantly increase the noise for a singles transmission source such as ^{137}Cs. Although not hydroscopic, LSO fluoresces when exposed to ambient light, and therefore must be encased in a light-tight package.

Gadolinium oxyorthosilicate (Gd_2SiO_5:Ce) or GSO is a strong competitor to both BGO and LSO. With a density of 6.71 g/cm^3 and a Z_{eff} of 59, the effective path length of 511-keV photons is 40% greater than with BGO. One of its major advantages is the decay time, which is only 60 ns and provides this scintillator with excellent timing resolution, capable of handling the high count rates in 3D-only PET scanners. This crystal is not hydroscopic and possesses good mechanical properties for cleaving. The intrinsic energy resolution at 511 keV is 9%, similar to that of NaI:Tl. This renders GSO a good material for scatter rejection, for prompt gamma rejection (relevant for some of the long-lived PET tracers, e.g., ^{124}I and ^{86}Y), and for singles-based attenuation correction with ^{137}Cs, in spite of its much lower fluorescent photon yield. Crystals contain no abundance of radioactive gadolinium isotopes, unlike lutetium-based crystals. Also the light output of GSO changes by only 1% per 10°C change in temperature, rendering this detector material extremely stable in all types of working environment. For these reasons, GSO detectors will be used on the latest commercial generation of Philips PET scanners (the Allegro and Gemini) [29].

Lutetium gadolinium oxyorthosilicate ($Lu_{1.8}O_2SiO_3$:Ce) or LGSO, produced by Hitachi, is a strong alternative to BGO and LSO. A Ce^{+3} ion activator is responsible for the very efficient luminescence. The energy resolution of LGSO has been measured at 12.4% [24], slightly poorer than LSO owing to the 25% reduction in light output. Also, the sensitivity parameter $\rho Z_{eff}{}^4$ is slightly less than LSO. LGSO has the advantage of a lower yield of radioactive Lu in comparison with LSO. The LGSO (Hitachi) demonstrated a decay time constant in the range 45–220 ns, depending upon the chemical composition.

Lutetium aluminum perovskite ($LuAlO_3$:Ce) or LuAP is a scintillator material useful for small animal PET tomography. Advantages of this material are the excellent ratio of number of emitted photons to the decay time, 11,200/ns per 511-keV photon, and its high density, 8.3 g/cm^3. A detailed study of the complex electron traps and scintillation mechanisms of this material can be found in Wojtowicz et al. [30]. Timing resolution as short as 160 ps was achieved when this detector material was irradiated with a ^{60}Co source and coupled to a PMT [31]. Comparative studies between LuAP and LSO coupled to avalanche photodiodes have demonstrated similar timing properties. However, LuAP has three times less light output than LSO. The time resolution was 680 ps for ^{60}Co and 1.16 ns for 511-keV photons. These characteristics obtained with an avalanche photodiode make LuAP a perfect choice for small animal compact PET tomographs based on photodiodes [27].

Yttrium aluminum perovskite, YAP or $YAlO_3$:Ce, is a newly developed scintillation material with considerable promise for nuclear medicine applications, especially for small animal imaging (see section "PET development for animal studies and their evolution"). YAP is a high-density, medium *Z* scintillator with a high light output, a short decay constant, and a characteristic wavelength which is closely matched to the spectral response of most photomultipliers. Furthermore, it is robust, chemically inert, and has a high melting point. Its main disadvantage is the low photofraction, which does not recommend it for clinical PET.

In spite of the rich assortment of inorganic scintillators now available, there is a continual search for new inorganic scintillator materials. This search is based on figures of merit (FOM), which combine all the required parameters to optimise PET scanner performance mentioned above. The FOM compares all scintillator parameters relative to the performance of BGO. Proposed software to assist in the search for new crystals and an extensive database of available scintillators are available [32]. Others are focusing on first principle calculations of scintillator properties using quantum chemistry cluster calculations [33]. As a part of the Crystal Clear Collaboration at CERN, many groups are working on new scintillator development with a better combination of price/performance. One objective is the replacement of expensive Lu or at least reduction of its composition fraction by replacement with another heavy cation. Introduction of a second heavy cation in the host matrix, such as Hf, Zr, or Ba (e.g., $La_2Hf_2O_7$ or $Ba_3Lu_4O_9$), with Ce^{+3} as an activator, has allowed the growth of crystals with high luminosity and speed with an increased average Z_{eff} of about 65 and a density of approximately 8 g/cm^3. These scintillators have maximum wavelength spectra shifted to the green region, which makes them promising for application with silicon photodiodes [34].

Special efforts have also been made to find inorganic scintillator materials that are compatible with Si− pin diodes (PD), i.e., emitting in the wavelength range of 550–1,050 nm. The most luminous compounds with appropriate Z_{eff} and high luminosity at the required wavelength have very long decay times of more than 100 µs, rendering them of limited utility for PET applications. Examples of such scintillator materials are Hg_2Cl_2 and $GdTaO_4$:Tb [19]. Only CsI:Tl has a relatively suitable emission spectrum with a decay time of about 1 µs. This material is suitable for modelling of PET detector modules with silicon photodiodes (SiPD).

Table 2 presents the most typical scintillators and their parameters, relevant for commercial and small animal PET applications. More information on scintillator properties for PET application can be found in van Eijk [35] and Melcher [15].

Radiation detector modules for PET applications and their readout

Conventional block modules with PMT readout

The main requirements for PET detector modules can be found in [36]. A successful PET detector module must identify 511-keV photons with: high efficiency (more than 85%), high spatial resolution (better than 4 mm FWHM), low cost (less than $401 cc), low dead time, good timing resolution (less than 5 ns FWHM for conventional PET), and good energy resolution (less than 20%).

The basic unit of PET detectors used in commercial and small animal imaging scanners is the crystal block. The block architecture provides a means of improving the detector packing fraction, which would be lost if miniature individual crystal elements were used, with minimal loss to positional resolution and adequate fluorescent photon statistics. This is achieved by scoring (partially sawing) the scintillator block into multiple pseudo-individual crystals. The scores provide a barrier to the optical dispersion of light between the individual elements of the crystal block.

The light collected from the block is converted into a measurable electrical voltage pulse on commercial PET scanners by photomultiplier tubes (PMTs). These devices convert the scintillation light into a very weak picoampere electrical signal at the photocathode, which is then amplified through an efficient low noise avalanche cascade process. They consist of a vacuum tube, of 15 mm or greater diameter, with a series of dynodes (electrodes) maintained under the control of a voltage divider (tube operating voltage of 800–1,500 V). Electrons released from the photocathode are accelerated through this voltage gradient to the first dynode, where upon collision they eject a greater number of electrons back into the vacuum tube. From this dynode, the electrons are accelerated in the direction of a second dynode from where an even greater number of electrons are ejected. This process repeats until amplifications of the initial voltage pulse of $>10^5$ are achieved. The high gain, stability, and low noise of the PMT have rendered it the standard scintillation light amplifier from the inception of gamma cameras through to today. The width of the PMT output pulse is determined by the statistical spread in the electron cascade process, frequently described by either a compound Poisson or Polya distribution [37], and is typically about 8% [38]. Thus voltage pulse width decreases with increasing scintillator quanta per event. The linearity of the PMT (except at very high pulses or operating gains) is the reason for their success in energy discrimination by the pulse height analyser. As a consequence, energy resolution is poorer for scintillators of lower light yields. The timing response of a PMT is of the order of 20 ns. Thermionic noise[4] limits the application of PMTs at very low count rates or X or gamma ray energies, but these are not problems in PET applications.

The most common detector configuration used in commercial scanners today couples each detector block with four PMTs with light sharing. The light collection efficiency of the PMT array is different for each elemental detector. In this way, it is possible to discriminate the detector element in which the most energy is deposited, whether produced by a single photoelectric event or via Compton interactions within different regions of the block. If the signal from the four PMTs are A, B, C, and D respectively, then the (x,y) location is determined by a simple analog ratio $x=(A+B)/T$ and $y=(A+C)/T$, where T is the summed signal $A+B+C+D$. This summed signal T is also used to estimate the total energy deposited within the block for the purpose of energy discrimination. Block sizes and individual elements vary between PET manufacturer requirements. For example, the blocks used in the HR+ (CTI, Knoxville, TN) consist of an array of 8×8 detector elements (64 total).

The development of multianode position-sensitive photomultiplier tubes (PSPMTs) of square shape allows accurate positional and energy information to be derived from the PMT itself. These devices utilize the positional information of the electron ejection site from the photocathode, which are steered into different compartments/chambers within the PMT tube. The spatial integrity of the avalanche clouds is maintained by the use of dynodes with special channels/perforations that maintain the focus of the electron path. These read-out systems work well with conventional detector blocks as well as pixellated crystal detectors (individual crystals mounted in an array conformation), where the smaller light dispersion can yield improvements in the spatial and energy resolution. PSPMTs operate well for most of the commonly used PET detectors, with emission wavelengths of less than 480 nm, e.g., BGO, GSO, and NaI:Tl. For a description of the design and performance characteristics of these devices, the reader is referred to the Hamamatsu website (http://usa.hamamatsu.com/hcpdf/parts_R/R7600- 00-C12.pdf).

Solid state detectors for PET applications

The typical intrinsic spatial resolution of PET cameras based on PMTs is 3–10 mm FWHM. This is limited by the scintillator PMT block design and the low quantum efficiency of PMTs. To achieve a higher spatial resolution, a higher segmentation of scintillators is required with the ability to readout each segment independently.

Although no commercial clinical PET camera to date uses semiconductor radiation detectors, these devices are promising as a means of overcoming the drawback of PMT-based PET instrumentation. Solid state photodiodes, in contrast to PMTs, are small, operate at much smaller voltage, and exhibit higher quantum efficiencies. This allows the possibility of easy read-out patterns of the sensitive area, especially through the introduction of monolithic pixelated photodetectors, permitting advanced PET detector modules packaging. The rapid developments of the microelectronic industry during last three decades have yielded high-purity detector grade silicon resulting in the ability to manufacture customized low-noise silicon planar photodetectors. The most important of these for PET applications are silicon p-i-n photodiodes (PDs), avalanche photodiodes and silicon drift photodetectors. In this section, we will briefly outline the principle of operation of these photodetectors and the main factors influencing their performance relevant to PET applications.

Principles of operation of silicon photodetectors

Semiconductor photodiodes are based on the p-n junction, which is produced by diffusion or implantation of boron into an n-Si high-resistivity substrate (p^+ layer). The back side of the substrate is diffused or implanted with phosphorus to produce a non-rectifying contact (n^+ layer). Figure 6 shows a cross-section of a typical Si p-i-n diode photodetector. Under reverse bias (negative voltage to the p+ side of the p-n junction relative to the n+ side) such structures conduct only a very small current relative to the forward biased p-n junction. Under reverse bias, all free majority charge carriers on the p-n junction leave the p^+ and n^- regions to form a depletion layer. The depletion layer consists of a space charge of ionized shallow impurities (donors in the case of n-Si)

---

[4] Thermionic noise is the spontaneous emission of electrons from the photocathode. For a bi-alkali photocathode at room temperature, approximately 100–1,000 electrons/cm^2 · s are produced, corresponding to dark currents of between 16 and 160 pA.

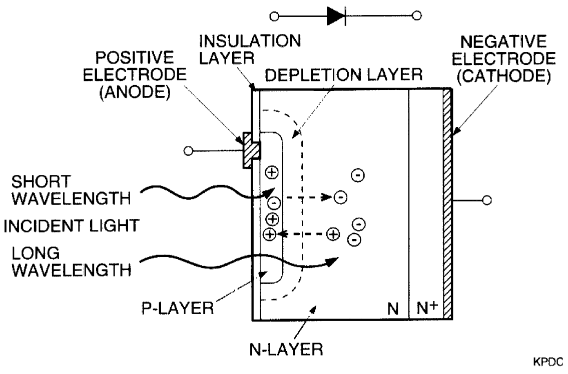

Fig. 6. Schematic diagram of reverse biased semiconductor photodiode. Shorter wavelength photons will be absorbed near the surface, creating more complicated conditions for the achievement of good quantum efficiency. (Picture from Hamamatsu Si photodiodes catalogue N KSPD0001E01)

situated between the majority carrier p and n regions within the crystal matrix. This space charge causes a strong electrical field from the p^+ to the n^- side of the depletion layer W, which decreases linearly from 2 V/W near the p^+ region to zero at the end of the depletion region. Increasing the reverse bias across the junction will increase the width of the depletion region as $W-(\rho V)^{0.5}$, where ρ is the resistivity of the silicon substrate and V is the magnitude of the reverse bias. For example, for a silicon substrate of thickness 0.35 mm with a resistivity of 5 kΩ/cm, 50 V is required to achieve full depletion of the photodiode, i.e., for the depletion region extending to the rear side of the detector. A further increase in the reverse bias will increase the electrical field within the detector. The minority charge carriers under these conditions will produce a very small bulk current. Special technologies are used to decrease the surface leakage of photodiodes, e.g., passivating with silicon oxide or producing guard rings outside of the sensitive area of the PD. To reduce the noise (leakage current) of a PD requires reduction of the capacitance (increasing the depletion layer width) and the reverse current. To satisfy both conditions the resistivity of silicon needs to be increased to deplete the PD at lower bias as well as to reduce the surface leakage of the PD.

When light photons strike a PD they produce e-h pairs in a depletion region, provided the photon energy exceeds the energy of the band gap. For silicon, this energy is about 1.1 eV, corresponding to a wavelength of less than 1,000 nm. For typical PET scintillators, the photon wavelength is in the range of 300–600 nm. A strong electrical field collects the e-h pairs produced in the depletion layer, thereby inducing a charge at the input of a charge-sensitive preamplifier which is proportional to the intensity of scintillating light, i.e., the radiation energy deposited in the scintillator [37, 38]. Silicon p-i-n photodiodes are robust, small, and inexpensive, operate at potential differences <50 V, are insensitive to magnetic fields, and exhibit very high quantum efficiencies, with a stable gain versus temperature and applied operating bias. Drawbacks are their relatively high electrical noise and their unity gain compared to a PMT.

Further development and improvement of semiconductor photodetectors has resulted in the avalanche photodiodes (APDs). These devices produce an internal amplification of the induced charge. An APD is also a p-n junction diode, but compared with p-i-n diodes, APDs are operated under much higher reverse bias. The physics of operation is based on the impact ionisation of Si atoms by the photoelectrons generated in the depletion region. These devices must be operated at a bias sufficient to accelerate the photoelectron to energies capable of ionising an Si atom. The manufacture of such p-n junctions requires special technology with the ability to produce a narrow (about 3 μm) region able to sustain a very high electrical field (avalanche region) at a surface depth of about 25 μm. New charge carriers produced in the avalanche region will gain enough energy from the strong electrical field to cause further impact ionisation. A charge amplification coefficient M is possible in the order of 10^3 in a modern APD, which is a function of the applied reverse bias [38].

The advantage of APDs for PET applications is the high S/N ratio due to the high gain, and the faster response relative to PMTs and PDs. APDs can also be produced as an array, greatly facilitating compact read-out systems. One drawback of APDs is that they require a much higher and stable bias. As a consequence, small changes in temperature can affect the bias and gain of these devices.

Silicon drift detectors are based on p^+-n junctions produced on both sides of silicon wafers with peripheral depletion layers which touch each other under reverse bias [39]. In this device, the photoelectrons drift through the bulk of substrate towards the n+ anode under control of the electrical field lines parallel to the wafer surface, whereas the holes drift more rapidly to the p^+ electrode under the control of the vertical component of the electrical field perpendicular to the wafer surface. The n^+ anode can be produced with a very small area, thereby yielding a device with a very small capacitance and low noise. An excellent review on all types of modern radiation detector has been provided by Lutz [40].

In PET applications, the overall system energy resolution is governed by the photodetector, PMT, PD, or APD [41, 42, 43], and the associated preamplifier electronic noise as well as by the intrinsic (and statistical) energy resolution of the detector material itself. The development of low-noise PD and APD arrays for PET application and PET detector modules is underway at several laboratories. Low noise and high quantum efficiency are the most important requirements for a PD because of the unity internal gain. Another complication is the short 0.1–0.2 μm absorption length for 400-nm wavelength light in silicon. The Lawrence Berkeley Laboratory group has developed a low-noise, high-quantum efficiency 8×8 array of 3×3 mm^2 PDs for coupling to pixelated LSO [44]. A special AR coating, transparent over the 4,000–1,000 nm wavelength and based on a polysilicon layer covered by indium tin oxide, allowed the production of an ideal optical entrance window with a quantum efficiency of about 70% for 420-nm light with a low series resistance electrical contact. The low-noise 140 electrons rms measured at room temperature, which resulted in an energy resolution of about 11% with a CsI(Tl) detector (4 µs time constant), was due to the low 50-pA leakage current and 3.2-pF capacitance per pixel under full depletion. Improvement in energy resolution and timing resolution is an issue in silicon PDs (Si PDs) for PET application. Several groups have reported on the timing resolution obtained with Si PD coupled to LSO [45,46]. For a single Si PD LSO detector module with a 250-ns shaping time constant and zero energy threshold, a 7-ns FWHM timing resolution was measured with a PMT. The coincidence timing spectrum for LSO coupled with the same photodiode detector module, at 511 keV from a ^{22}Na source, exhibited a timing resolution of 35 ns FWHM [47].

Another promising alternative is silicon drift photodetectors (SDDs). An advantage of SDDs is the very low capacitance, and hence low noise, which is independent of the detector area. However, they are currently relatively slow, although PET-oriented development is now channelled on improving both the energy and the timing resolution for this class of devices. The 8×8 array of SDD 2×2 mm^2 pixels was cooled to −30°C and demonstrated noise levels as low as 26 electrons rms with an energy resolution of 13% FWHM for 662-keV gamma photons. The coincidence timing resolution was reported at 13 ns FWHM. The quantum efficiency for 430 nm was 40%, which is double the value obtained with PMTs but lower than that currently achievable with PD arrays. New developments will include integrated junction field effect transistors with expected timing resolutions of the order of 2 ns. Such modules can be cooled relatively easy using a Pelletier cooler [48].

Comparative studies of PDs, APDs, and SDDs using a CsI(Tl) detector exposed to 662 keV ^{137}Cs gamma rays demonstrated that the SDDs and APDs had a better energy resolution (6.6%) relative to the PMT (7.1%), but that PDs had a slightly inferior energy resolution, at 7.9% [49]. The large detection area of SDDs makes them attractive for PET application with improved timing resolution. The excellent quantum efficiency of PDs, together with their low cost, makes them ideal candidates for high spatial resolution PET application with lower activity animal scanners.

New developments utilizing multipixel hybrid photodiodes (M-HPD) coupled with optical fiber lightpipes to form discrete 2×2×10 mm^3 LSO elements and parallel readout demonstrated a time resolution of less than 4 ns. Advances in APD arrays dedicated to PET applications are being developed by several groups and are an attractive alternative to PSPMTs. The first APD PET detector modules were evaluated at the University of Sherbrooke [50]. Further examples include APDs produced by the company RDM; these include 4×4 to 14×14 arrays with 2×2 mm pixels, as well as an 8×8 array with 1×1 mm pixels on NTD silicon [51]. New APDs are working at a wide range of bias voltages with demonstrated gains of up to 1,500 at a bias of 1,800 V. The gain variation in these APDs was measured at about 2.5%/°C. Timing resolutions of 2.8 ns for LSO/APD and PMT/LSO, with energy resolutions of 12% FWHM and a quantum efficiency for LSO light of about 65%, have been achieved. A 32-channel 4×8 array with sensitive pixel area of 1.6×1.6 mm^2 and pitch 2 mm has been produced by Hamamatsu Photonics [52].

Further advances in p-i-n PDs and SDD arrays for PET application, with improvement in the S/N ratio achievable with integrated junction field effect transistors on the same high-resistivity silicon, have been produced with an anticipated timing resolution of 2 ns [53].

Detector module design with depth of interaction capability

Limitations of current PET detector module design

Improvement in PET image resolution can be achieved by reducing the cross-sectional area of each scintillator element. However, to achieve this and not adversely affect detector sensitivity, crystals need to remain about 30 mm in length. Long small cross-sectional crystals can worsen the charge collection efficiency and hence result in a deterioration in the S/N ratio and timing properties. In addition, such crystals increase the rate of radial image degradation away from the camera "sweet spot." This phenomenon is referred to as the "*depth of interaction*" (DOI) problem. Several different approaches to overcome these problems have been proposed based on PSPMT, Si PDs, and APDs and these will be discussed in this section.

Commercial cameras have a detector ring which is larger than the transaxial field of view of the scanner. The detector modules of these designs set the point of 511-keV photon interaction at a point corresponding to the center of a scintillator crystal defined by the read-out logic. This technology is resolution limited at the edges of the field of view because the line of response of two such photons can be miscoded by an amount proportional to the angle of incidence of the 511-keV gamma ray to the axes orthogonal to the detector ring (Fig. 7). This effect, known as the parallax error, becomes worse as the ring diameter is reduced, and as the cross-sectional area of the detector is made smaller. This deterioration in image resolution with distance from the ring axis can be reduced (or eliminated) through a measurement of the

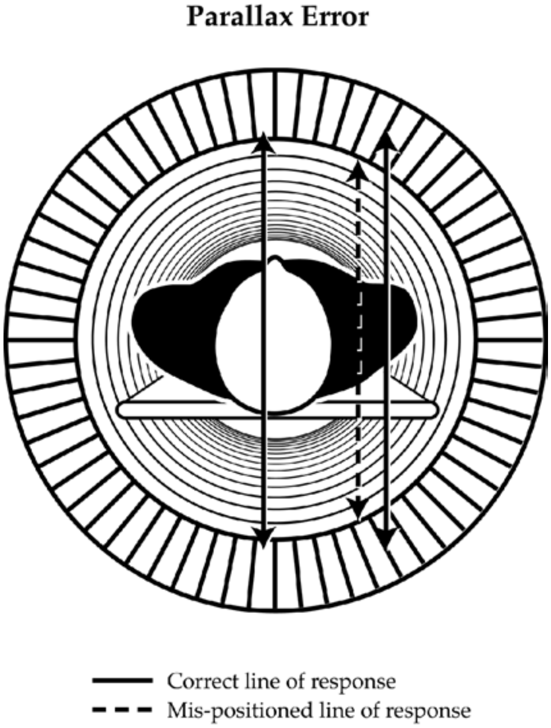

Fig. 7. The parallax or depth of interaction problem associated with decays at the edge of the transaxial field of view of a PET scanner

depth of interaction (DOI) within the scintillator. It is most important for 3D PET where a DOI capability would allow a combination of position-independent spatial resolution and high sensitivity.

Whereas no commercial PET scanner is currently able to perform DOI corrections, efforts are underway to design PET read-out modules with this capability, because of the potential improvements in whole-body PET imaging. There are three main research directions for performance of DOI measurements: dual photodetector readout, phoswich detectors, and segmented crystals.

Dual photodetector readout PET modules

This approach, first proposed by Moses et al. [54], is based on a pixelated array of 3×3×30 mm of BGO crystals coupled at one end to a single PMT and at the opposite end to an array of 8×8 Si pixelated 3×3 mm Si PDs. The PMT provides the accurate timing pulse and energy resolution and the PD array defines the crystal of interaction. This PET detector module is based on light sharing between the PD and PMT for each BGO pixel. The DOI is determined from measurements of $A_{PD}/(A_{PD}+A_{PMT})$ for each crystal of interaction, where A_{PD} is the photodiode pulse height and A_{PMT}, the pulse height observed by the PMT, rescaled to an equivalent amplitude to match the PD. The initial tests were performed with a single BGO crystal of 3×3×30 mm [55], cooled to a temperature of –20°C to increase the BGO light output. A DOI resolution of 5–8 mm was achieved, depending on how close the 511-keV photon interactions were to the PD side of the detector. The fraction of misidentified DOI events depended on the S/N ratio and the noise spread between the individual PDs in the array. Even with good S/N ratios, the misidentification fraction was observed to be about 25% for this module. Improvements in DOI measurements are achievable through the use of the higher light output crystal LSO. Calibration of such a module could be performed with a side incident beam; however, this would require removal of the detector module from the gantry. Another approach to calibration is based on Monte Carlo simulations of photons approaching from the PD side, and assuming that light collections from the scintillator pixels is linear with depth. This method would offer an in situ DOI calibration estimated to take 2–3 h for a 30,000 crystal PET tomograph [56]. Recently, a functional prototype of such a PET detector module was realized at the Lawrence Berkeley Laboratory [57] utilizing customized integrated circuit readout of the PD arrays. The energy resolution determined from the sum of PD+PM signal was 25%, and the DOI resolution was 6–15 mm FWHM. Other designs of PET modules, which use analogue signals, whose amplitude depends on the DOI, are currently under evaluation [58, 59, 60].

The double photodetector approach for a PET detector module with DOI capability was reported based on a PSPMT optically coupled to a pixelated 2×2×21 mm^3 LSO crystal with a side of each LSO pixel optically connected through bent optical fibres to a single-channel PMT, which is outside the field of view [61]. Using the same principle of DOI measurements as described above, the possibility of achieving DOI resolutions from 4.2 to 6 mm was demonstrated. The advantage of this design is the very good timing capability and improvement in the S/N ratio, providing better accuracy for the DOI measurements. The major drawback of this design is the decrease in sensitivity due to attenuation in the optical fiber and the reduction in the gantry opening (by up to 5 cm) to accommodate the space for bent optical fibers [62].

Phoswich and light-sharing detector modules

This type of PET detector with DOI measurement capability is based on the pulse shape analyses of scintillating light emitted from two or more stacked scintillators with different decay times. The different scintillator decay constants provide the basis for timing discrimination, thereby allowing determination of the scintillator layer of the initial photon interaction. Detector blocks have been made utilizing one layer of BGO crystal and another of GSO [63]. The disadvantage of using a BGO and GSO pair is the different light output of the scintillators and the long decay of BGO in comparison with GSO scintillators.

Another approach is based on using GSO(Ce) scintillators with different concentrations of Ce, (higher dopant concentration increases its speed) so as to alter the decay time of the two layers, yet maintain similar light output [64]. The PET detector module with stacked 2.4×2.4×6 mm^3 GSO crystals in the DOI direction were coupled to a PSPMT. Experiments demonstrated a small degradation in the efficiency of the light collection from the top to the middle of the crystal, which was 60% and 80%, respectively, relative to the bottom one. In such a PET module, the optical coupling between separate stacked crystals is critical for functional DOI operation.

Phoswich detectors can be used for the separation of events from two crystals either in the time domain as described above or in the energy domain by pulse height analysis. Inadama et al [65] describe a phoswich PET module with DOI capability for couples of LSO/LSO at different Ce concentrations, LSO/GSO, and NaI(Tl)/LSO. LSO yielded different light intensities that could be used for crystal identification by arrangements of two or more energy windows to isolate distinct photo peaks and thereby identify the crystal of interaction. This method has disadvantages due to the possible contribution of scattered photons from the high light to the low light yield crystal. Application of time discrimination techniques allows discrimination of scattered events in timing spectra since they will be positioned between distinct peaks. For a comparison of the two methods, the reader is referred to Inadama et al [65].

Another design of Phoswich detector module has been reported, which consists of four blocks of GSO scintillator, each block consisting of four stages of 2×2 array of 2.9×2.9×7.5 mm of GSO [66]. The four-stage DOI detector is achieved by using GSO with decay times of 60 ns and 35 ns in consecutive blocks. Time-discrimination techniques with 2D position image histograms of light sharing in each block measured by a 4×4 PSPM (2×2 anodes for each block) were used to discriminate the crystal of interaction. This design of PET detector module can be constructed with the same crystal elements and does not require an additional photodetector.

Asymmetrical light-sharing techniques in the construction of multistage 3D crystal PET modules coupled with a PSPMT showed good results in identifying the crystal of interaction, without using time discrimination, but only a 2D positioning map [67]. Such special patterns of light sharing can be achieved by using air gap and reflective tape between the crystal elements. The data acquisition of such modules is acquired in list mode with retrospective analysis for the correlation of events in amplitude and position. Of particular importance in the mass production of PET detector modules with DOI capability is the need for identical optical coupling between the different stages of crystals, so as to ensure an equal light attenuation at the interfaces between stages. This is critical to avoid deterioration of energy resolution and consequently an increased misdetermination of the DOI. LSO and GSO are preferred for DOI applications since these scintillators provide a sufficient light yield for the required energy and temporal resolution. Methods of separation of segmented crystals, based only on photopeak amplitude discrimination from each segment along its length, due to adjustment of inter-segment coupling, have also demonstrated future promise for DOI applications [68]. Another advantage of such detector modules is the ability to make use of the fact that most photon interactions occur in the front segment of the scintillator, allowing lower energy scattered photons from the patient to be readily discriminated and rejected by events confined within the front segment of the device.

Solid state detector PET modules

The development of low-noise pixelated PD and APD arrays has made them a highly suitable choice in the design of DOI-capable PET modules. Shao et al. [68] reported on the use of a 4×4 APD array with a 2×2 mm^2 pixel size and 0.4 mm spacing optically coupled from both sides of a 2×2×22 mm^3 LSO array. With amplification gains of about 1,000, a DOI resolution of 4.2–6 mm has been demonstrated. The advantage of such a design is that the same photodetectors can be used from both sides of the LSO array, promising uniform performance and allowing the signal to be summed without any additional scaling, thereby simplifying the energy and timing discrimination. Such a module has the additional benefit that the same readout electronics can be used for the whole module.

Measurements with the Hamamatsu 2×8 APD array of sensitive pixel size 3×3 mm and a pitch of 4 mm have been reported using a light-sharing technique from two segmented layers of 4×4×10 mm^3 LSO crystals offset with respect to one another by one-half of the crystal size in one or two dimensions [69]. Measuring the signal distribution in the APD pixels above the discriminator level allowed reliable identification of interaction between the bottom or top crystals.

New developments in PET modules for 3D measurements of the point of interaction based on a stacked design of sandwiches using LSO pixel arrays, Si PD or APD arrays optically coupled from the wide side of the bulk scintillator are continually advancing the feasibility of this field [69, 70]. The impact of these technologies on the future design of PET scanners will become known in the next 10 years.

PET instrumentation on the market

Dedicated whole-body PET scanners

For a history of the evolution of clinical PET scanners the reader is referred to Nutt [71]. Nutt suggests that the important landmarks in PET are the first human PET tomograph based on NaI(Tl) in 1974, the discovery of BGO in 1977, the development of the block detector in 1984, and the development of the LSO crystal during the 1990s. To place commercial scanners in perspective, most high-performance commercial PET scanners designed and built between the late 1980s and today have used BGO crystals because of the high sensitivity for 511-keV photons, cost, and availability. These have included the PC4096-15WB scanner [72] (Scandatronix, Uppsala, Sweden), the POSITOLOGICA [73], the ECAT EXACT [74], the ECAT HR+ [75], the POSICAM 6.5 [76], the new mPower PET scanner (webpage http:// www.positron.com), the GE Advance [77], the recent GE Discovery LS and ST combination PET/CT units (General Electric, Waukesha, WI webpage http://www.gemedicalsystems.com/rad/nm_pet/products/pet_sys/index.html), the CTI EXACT HR+, ART, and the REVEAL HD PET/CT unit (CTI, Knoxville, TN product webpage http://www.ctimi.com/ctimi/products/scanners. dtml). The physical performance characteristics of most of these commercial units, except for the latest, have been published as referenced above. A summary of the most important of these properties is shown for representative clinical PET scanners in Table 3.

Currently available scanners from CPS include the BGO-based ECAT line consisting of: (a) the EXACT, a 2D and 3D system, (b) the HR+ high resolution, which is also a 2D and 3D system, (c) the ART (a 3D-only scanner using rotating BGO detector modules designed to economize on crystal material), and (d) the REVEAL HD, a scanner that combines the HR+ (or EXACT) with a Siemens CT scanner (from single to 16 slice). Scanners (a), (c), and (d) are also available with LSO crystals as the ACCEL, EMERGE, and REVEAL RT. General Electric Corporation provides a range of exclusively BGO scanners consisting of the Advance NXi dedicated PET system and the Discovery LS and ST combined PET/CT units. Philips also provide three separate PET products: the C-PET Plus, which is an NaI:Tl curved panel-based dedicated PET scanner, the Allegro, a GSO scanner, and the Gemini, which combines the Allegro PET scanner with a Philips MX8000 D multislice CT scanner.

The changes, which have occurred over the past 15 years, have been mostly incremental: a wider patient port (the evolution from brain scanners to whole-body scanners), increases in the number of detectors, improvements in block design, faster electronic signal processing, advances in computer hardware and software, and, of course, the recent introduction of new detector materials. As a consequence, there has been a continual improvement in sensitivity and resolution and, therefore, image quality.

Interest is rapidly increasing in PET, but even more so in combined PET/CT units, owing to the greater ability to interpret the PET scan when co-registered with anatomical image data. In addition to its application in disease diagnosis and staging, PET/CT is beginning to play a major role in intensity-modulated radiation treatment planning (IMRT). Partially to fulfil this need, PET/CT scanners have been designed with larger patient apertures to allow the imaging of patients within radiotherapy immobilization casts. Most dedicated PET scanners have patient apertures of 58–62 cm. The first commercially available combined PET/CT scanner, the Biograph (CPS) (which appeared in 2001), consisted of a flush 70-cm bore unit with a redesigned patient transport system to carry the patient through both units without differential table sag, vital to accurate PET/CT image registration. The first PET/CT scanner by GE, the Discovery LS, combined the 58-cm bore Advance NXi PET scanner with a 70-cm bore multislice LightSpeed CT scanner. The recently released GE Discovery ST also has the advantageous contiguous 70-cm bore PET/CT unit. The Philips Gemini comprises the GSO Allegro (62-cm bore) with a 70-cm MX8000 D multislice CT scanner.

System sensitivity is considered the most important parameter since it determines the image quality per unit scan time or alternatively the time required to perform a whole-body scan. The physical definition is the ratio of the number of detected events to the number of decays within the scanner field of view. On a clinical system, sensitivity depends principally on three main factors: First, it depends on the detector material, which ranks in the order: BGO, LSO, GSO, NaI:Tl. Second, it depends on the axial field of view of the camera since this determines the length of the body segment that can be imaged per bed position. Although it is desirable to have a longer axial field of view, this adds significantly to the complexity and cost of the scanner. The axial field of view of modern PET scanners is 15–16 cm, with the exception of the C-PET, which has an axial field of view extending to 25.6 cm. Third, it depends upon whether the scans are acquired in 2D or 3D mode. Scanner sensitivity is substantially greater in 3D versus 2D mode owing to the wider acceptance angle of coincidence events through the inclusion of oblique lines of response. Although there are more true events, there is a marked increase in scatter and random events. The increase in scattered events results in a degradation of image contrast. The scatter fraction is independent of the activity within the patient, but is dependent on the patient girth. Of greater concern in 3D imaging are the random coincidences arising from uncorrelated decays. Random events increase at a rate corresponding to the count rate (or patient activity) squared. For low activities, randoms contribute only a small fraction of the signal. In a 2D acquisition, doubling the patient activity from 200 to 400 MBq practically doubles the study count rate (Fig. 8). In a 3D acquisition, the count rate becomes progressively non-linear beyond about 150 MBq administered activity (for a BGO scan-

Table 3. Performance characteristics for the current commercial clinical PET scanners

	CTI ECAT Exact (922)	CTI ECAT HR+	CPS Accel	GE Advance	GE Discovery LS PET/CT	GE Discovery ST PET/CT	C-PET	CPS BGO PET/CT	CPS LSO PET/CT	Philips Allegro/ Gemini PET/CT[a]
Crystal	BGO	BGO	BGO	BGO	BGO	BGO	NaI:TI	BGO	LSO	GSO
Patient port	56.2 cm	56.2 cm	56.2 cm	58 cm	59 cm	70 cm	62 cm	70 cm	70 cm	56.5 cm
Total no. of blocks	144	288	144	168	168	280	N/A	288	144	28
No. of crystal detectors/block	8×8	8×8	8×8	6×6	6×6	6×6	N/A	8×8	8×8	22×29
Crystal size										
Transaxial	6.39 mm	4.39 mm	6.45 mm	4.0 mm	4.0 mm	6.2 mm	47 cm circum.	4.39 mm	6.45 mm	4 mm
Axial	6.39 mm	4.05 mm	6.45 mm	8.0 mm	8.0 mm	6.2 mm	30 cm	4.05 mm	6.45 mm	6 mm
Radial	20 mm	30.0 mm	25 mm	30.0 mm	30.0 mm	30.0 mm	2.54 cm	30.0 mm	25 mm	20 mm
No. of detector rings	24	32	24	18	18	24	N/A	32	24	
Detector ring diameter (cm)	82.4	82.4	82.4	92.7	92.7	88.0	62.0	82.4	82.4	90
Total no. of detectors	9,216	18,432	9,216	12,096	12,096	10,080	Six curved NaI:Tl	18,432	9,216	17,864
Transaxial field of view (cm)	58.5	58.5	58.5	50	55	60	57.6	58.5	58.5	57.6
Axial field of view (cm)	16.2	15.5	16.2	15.2	15.2	15.2	25.6	15.5	16.2	18
Slice thickness (mm)	3.375	2.46	3.375	4.25	4.25	3.23	4.0 (body)	2.43	3.4	2
No. of slices	47	63	47	35	35	47	64	63	47	90
Coincidence timing window (ns)	12	12	6	12	12.5	11.7	8	12	6	8
Coincidence timing resolution (ns)	6	6	3	6	6	6		6	3	4
Energy window width (keV)	350–650	350–650	350–650	300–650	300–650	300–650	435–665	350–650	350–650	
Sensitivity 2D trues, NEMA 94 phantom (kcps μCi^{-1} cc^{-1})	180	200	200	217	146	300	N/A	N/A	N/A	N/A
Sensitivity 2D trues + scatter, NEMA 94 phantom (kcps μCi^{-1} cc^{-1})	214	244	238	238	159	348	N/A	N/A	N/A	N/A
Sensitivity 3D trues, NEMA 94 phantom (kcps μCi^{-1} cc^{-1})	780	900	925	1,261	838	1,280	444	1,049	999	>700
Sensitivity 3D trues + scatter, NEMA 94 phantom (kcps μCi^{-1} cc^{-1})	1,218	1,406	1,445	1,941	1,297	1,800	592	1,586	1,514	>1,000
2D axial resolution (mm)							N/A	N/A	N/A	N/A
FWHM at 0 cm	4.5	4.2	4.3	4.2	4.0	5.0				
FWHM at 10 cm	5.9	5.0	6.0	5.5	5.4	6.5				
FWHM at 20 cm	N/A	6.8	N/A	7.4	6.6	N/A				
3D axial resolution (mm)										
FWHM at 0 cm	4.6	3.5	4.7	6.0	6.0	5.0	6.2	4.2	5.8	4.2
FWHM at 10 cm	6.5	5.3	7.1	6.3	6.3	6.5	6.9	5.7	7.1	5.6
FWHM at 20 cm	N/A	7.8	N/A	6.6	6.6	N/A	8.0	N/A	N/A	N/A

Table 3. (continued)

	CTI ECAT Exact (922)	CTI ECAT HR+	CPS Accel	GE Advance	GE Discovery LS PET/CT	GE Discovery ST PET/CT	C-PET	CPS BGO PET/CT	CPS LSO PET/CT	Philips Allegro/ Gemini PET/CT[a]
2D transaxial resolution (mm)							N/A	N/A	N/A	N/A
FWHM at 1 cm	6.0	4.6	6.2	5.1	4.8	6.2				
FWHM at 10 cm	6.7	5.4	6.7	5.7	5.4	7.0				
FWHM at 20 cm	N/A	7.9	N/A	7.2	6.2	7.5				
3D transaxial resolution (mm)										
FWHM at 1 cm	6.0	4.6	6.3	5.1	4.8	6.2	5.7	4.5	6.3	4.8
FWHM at 10 cm	6.7	5.4	6.8	6.0	5.4	7.0	5.7	5.6	7.4	5.9
FWHM at 20 cm	N/A	7.8	N/A	7.4	6.2	7.5	N/A	N/A	N/A	N/A
Scatter fraction 2D (%)	16	18	16	9	9	16	N/A	N/A	N/A	N/A
Scatter fraction 3D, NEMA 1994 (%)	36	36	36	36	36	29	25	37	34	<30
Randoms = trues	345 kcps	570 kcps	850 kcps (3D) 330 kcps (HR)	486 kcps (HS)	460 kcps (HS)		Never achieved due to dead-time	679 kcps (3D)		119 @ 0.27 mCi
50% dead-time	345 kcps	635 kcps	850 kcps (3D)	474 kcps (HS) 289 kcps (HR)	505 kcps (HS) 304 kcps (HR)		38 @ 0.11 mCi	356 kcps (3D)	434 kcps (3D)	116 @ 0.24 mCi
Peak noise equivalent count (kcps)	25	38	60	40	40	62	49	38	44	48

HS, High sensitivity; HR, high resolution

[a] The results for the scatter fraction 3D and count rate performance of the Philips Allegro/Gemini PET/CT were obtained using the NEMA 2001 protocols

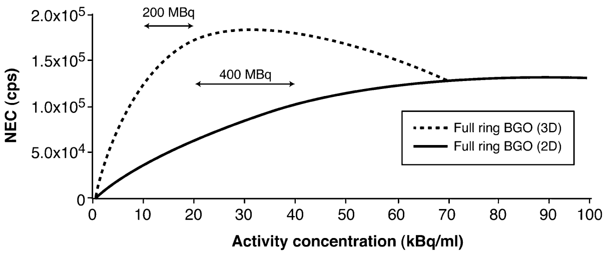

Fig. 8. Noise equivalent count rate curves, 2D versus 3D

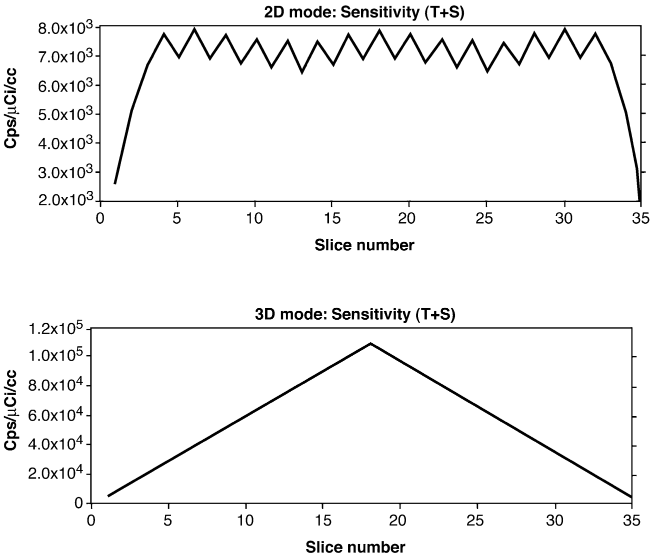

Fig. 9. Slice sensitivity versus axial position in 2D and 3D scans

ner).[5] In order to provide a physical measure with which to benchmark advances in PET camera performance, the concept of noise equivalent count rate (NEC) was introduced. The NEC is defined as:

$$\mathrm{NEC} = T^2/(T+R+2S)$$

where T is the true coincidence rate, R is the random coincidence rate, and S is the scatter coincidence rate.

An NEC curve provides a statistic which shows the dependence of the increase in trues on increasing activity in the field of view, yet is penalized by scatter and randoms, which provide inaccurate positional information about the source distribution and therefore degrade image contrast and quality. Figure 8 shows the typical NEC curve for a BGO PET scanner in 2D and 3D modes of operation. Note first that in 2D the camera response is linear over a much larger range of activities than for 3D and second, that there is always a point at high enough activities at which the NEC in 2D exceeds that in 3D. To shift the peak in the NEC curve for the 3D mode of operation to higher activities, faster scintillators are required, such as LSO or GSO. Moses [78] modelled the shift in the NEC curves for coincidence timing windows ranging from 12 to 4 ns and estimated that reduction in the coincidence timing window from the nominal 12 ns to 10, 6, and 4 ns would cause the peak in the NEC curve (in kcps $\mu\mathrm{Ci}^{-1}$ cc^{-1}) to shift (increase) by 8%, 31%, and 48%, respectively. This is the motivating factor behind the introduction of LSO and GSO detector blocks on new PET scanners.

Most PET scanner performance data in the published literature, including count rate performance, from which NEC is calculated, are for a 20-cm cylinder, as defined in the NEMA94 publication [79]. This standard was defined at a time when whole-body PET scanning was in its infancy, and it has recently been surpassed by the newer NEMA 2001 standard [80, 81]. This longer cylinder includes contributions to the randoms rate and scatter from out of field activity, and contains heterogeneous density inserts, rendering it more realistic in relation to whole-body patient studies. Badawi et al [82] measured the NEC characteristics for BGO cameras for a number of tissue-equivalent phantoms ranging in size from an infant's head to an obese patient's chest. This study demonstrated that the NEC, at a fixed activity, is reduced with increasing phantom/patient size when scanning in 3D mode, consistent with the clinical observations of obese patients. This group also investigated the effect of adjusting the lower level energy discriminator (LLD) setting from 150 to 500 keV, i.e., just below the 511-keV annihilation energy. The LLD setting that would yield the optimum NEC, at clinically relevant activities, was shown to vary from a 250-keV threshold for the smallest 13-cm-diameter phantom size to 400 or 450 keV for a 37 cm by 48 cm chest phantom. Current clinical PET practice is designed to maximize sensitivity using a fixed 300- or 350-keV LLD window setting and administered patient dose. Yet the total system counts in a study must maintain a balance between increasing the true coincidence counts, which provide the useful image data, and reducing scatter and random counts, which degrade it; it is in this area where patient-specific optimization of the acquisition parameters may yield gains in image quality. Use of the faster detectors such as LSO and GSO, which permit the use of a shorter coincidence timing window, e.g., 6 ns, improves the NEC curve because of greater randoms rejection. A significant reduction in the coincidence timing window for BGO would adversely affect scanner sensitivity. Another important factor in comparing 2D and 3D is the variation in sensitivity in the axial field of view (Fig. 9). In 2D, the sensitivity is a flat sawtooth in the axial direction corresponding to alternate direct and cross-plane slices. In 3D, the sensitivity corresponds to a triangular response peaked at the central slice. The reduction in slice sensitivity approaching the

---

[5] To convert from kBq/cc in a patient into an administered activity, divide by 10^3 to convert to MBq/cc, multiply by the patient weight 70,000 g, divide by the fraction of the torso body activity within the field of view (approx one-fifth) and divide by 1.5 to account for physical decay and patient clearance between the injection time and the scan time.

camera ends is the result of the linear decrease in the number of oblique lines of response that contribute to each respective slice. A clinical consequence of these axial response profiles is that 2D whole-body scans require only a single slice overlap between contiguous bed positions, whereas in 3D, an overlap corresponding to 10%–20% of the scanner axial field of view is necessary.

The resolution of a clinical whole-body PET camera ranges from 4 to 8 mm, and is symmetrical in the transaxial and axial planes. The large contribution of this resolution is due to the detector ring diameter, typically about 90 cm on commercial whole-body systems. This resolution is greatest at the center of the camera, "the sweet spot," because all gamma rays emanating from this point strike the detectors orthogonally. The resolution degrades as the source of activity moves towards the edge of the scanner owing to the depth of interaction (DOI) problem discussed in the section "Detector module design with depth of interaction capability". Therefore the resolution along the central axis of the patient is a factor of 2 higher than at the patient periphery, a feature of all current commercial scanners (Table 3). The quoted resolution of a PET scanner is defined by the FWHM of a line (or point) source measured at specific points within the field of view. This optimum resolution is measured for a stationary object, acquired with sufficient counts such that the statistics of the source imaged can be accurately fitted to a Gaussian distribution. The resolution of patient scans differs from this ideal in two ways. First, patients are subject to voluntary and involuntary motions. Second, the count statistics in clinical studies do not meet the accuracy constraints of a resolution phantom measurement. The former can be greatly mitigated using gating techniques, which are routine in cardiac imaging, but now have also been developed to compensate for respiratory motion [83]. Such methods improve PET image contrast, but at the expense of worsened count statistics. Count statistics are improved by higher system sensitivity, which impacts upon the clinical measured resolution and diagnostic accuracy. System sensitivity combined with resolution determines the minimum limits of detectability of a system, i.e., the smallest lesion that can be detected in a defined scan duration. A comparative study of several commercial dedicated PET scanners and coincidence gamma cameras was performed using an anthropomorphic phantom containing lesions comprising of ^{22}Na inserts [84]. Although this study was performed on scanners available before 2001, one clear conclusion was that dedicated PET scanners are greatly superior to the gamma cameras used in coincidence mode.

A principal factor affecting image contrast and image quantitation is the scatter fraction. This is a measure of the fraction of detected coincidence photons, for which at least one 511-keV photon has undergone scatter yet not been rejected by energy discrimination, thereby generating a mispositioned line of response. In 2D mode, scatter fractions are typically <10% (16% on the GE Discovery ST), depending on the thickness and design of the septa. Only photons scattered within the same axial plane can reach the detector ring, the remainder being absorbed by the septa. In 3D, the number of detected scatter events rises significantly. The 3D scatter fraction ranges from 25% to 36% using the 20-cm-diameter NEMA 1994 phantom, and can be 40–50% using the longer NEMA 2001 phantom, which makes provisions for out of field activity. In fact, the scatter fraction can be substantially greater than this (50–80%) in many clinical whole-body scans, such as the chest and pelvis of obese patients. To reduce the scatter fraction, detectors are required with higher energy resolution. Energy resolutions (FWHM) for BGO, NaI:Tl, GSO, and LSO at 511 keV are quoted as 18%, 7%, 9%, and 11%, respectively. The wide energy window widths used on most PET cameras (Table 3) is a trade-off between sensitivity and scatter rejection. Small angle Compton scattered photons contain some positional information and are commonly accepted at the expense of some contrast degradation. Improvements in detector energy resolution will provide the ability to maintain scanner sensitivity with improved scatter rejection. Better energy resolution will also benefit the image quality of certain longer-lived positron-emitting isotopes such as ^{124}I (4.2 days) and ^{86}Y (13.6 h), which emit concomitant gamma rays that cannot be discriminated by timing or energy resolution on the current scanners.

PET development for animal studies and their evolution

Radioisotope imaging of small animals, such as mice and rats, using high-performance PET and SPET, is becoming a valuable tool for studying animal models of human disease [85, 86, 87]. Over the last decade, the use of the mouse as a "laboratory" for genetic research has shown a dramatic increase owing to the widespread availability of transgenic and "knock-out" rodent models, designed specifically to evaluate gene function. The mouse has long been used by molecular biologists to study fundamental cellular events in vivo, but the relatively small size of the mouse (weight 20–30 g) makes it difficult to use imaging instruments developed for human subjects, i.e., the sensitivity and spatial resolution of such PET scanners are wholly inadequate for the quantitative and qualitative assessment of in vivo gene expression, and are even unable to differentiate between the internal organs of the mouse for drug biodistribution work. The need for improvements in sensitivity arises from the desire to image the expression of genes that are translated in only a few copies per cell (1 pM). Improvements in image resolution are also required if the heterogeneity of radiotracer uptake within tumor and normal organs is to be attained. In this context dedicated rodent nuclear imaging techniques [88, 89, 90] provide a powerful non-in-

Fig. 10. Photograph of the microPET (**a**), the YAP-(S)PET (**b**), and the HIDAC scanners (**c**)

vasive method to follow the temporal kinetics of pharmaceuticals in the same animal, without the need to sacrifice, dissect, and count, as in traditional pharmacokinetic and biodistribution studies.

Despite the high complexity and expense of current small animal PET scanners, the remarkable possibilities offered by these techniques justify the growing interest of many research groups all over the world in the development of better instruments. Many solutions have been proposed for the detection system. Detectors based on a matrix of scintillating crystals coupled to a position-sensitive photodetector are a well-established technology. Usually a PMT is used for the matrix readout, but in the future new photodetectors based on semiconductors, such as the hybrid photodiode (HPD) or avalanche photodiode (APD), could be used. The performance of the best scanners in terms of spatial resolution is better than 8 mm^3 FWHM, while the sensitivity ranges around 20 cps/kBq. While the spatial resolution is getting closer and closer to the intrinsic limit, a great increase in sensitivity is desirable so as to improve image quality (S/N ratio) and reduce scan time (thus making dynamic studies easier and more precise).

Dedicated instruments, characterized by high performance, have been produced, but most of these have been built as research prototypes. Three small animal PET scanners are commercially available: microPET4, designed and developed at UCLA, Los Angeles, and distributed by Concorde Microsystems Inc. (10427 Cogdill Rd, Suite 500 Knoxville, TN 37932, USA), the YAP-(S)PET, developed at the University of Ferrara and now distributed by I.S.E. [Via Nuova 128, 56010 Vecchiano (Pisa), Italy], which is able to perform both PET and SPET animal studies, and the HIDAC PET, produced by Oxford Positron Systems Ltd. (5 Landscape Close, Weston Business Park, Weston-on-the-Green, Oxon OX25 3SX, UK, http://www.oxpos.co.uk). Recently, Philips is also proposing a dedicated GSO PET scanner, for small animal imaging, that is a scaling of their clinical unit.

Two commercial versions of the microPET scanner (Fig. 10b) are produced by Concorde Microsystems Inc., one for imaging rodents (microPET R4) and the second for non-human primates (microPET P4). The Concorde microPET [91] detectors comprise an 8×8 array of 2.1×2.1×10 mm^3 etched LSO crystals coupled to a position-sensitive PMT (Hamamatsu R-5900 C8) via bundled 1 mm^2 fiber optics. The detectors are arranged on four rings. Each ring of the microPET R4 contains 24 of these detectors. The performance of the Concorde microPET R4 indicates a volumetric spatial resolution of about 8 mm^3 in the center of the field of view and a maximum sensitivity (for a 250-keV threshold) of 24.3 cps/kBq (900 cps/μCi). Further developments of this system, referred to as microPET II, promise a resolution approaching 1 mm^3 [92].

The YAP-(S)PET scanner [93] (Fig. 10a) is made up of four modules, each composed of 20×20 $YAlO_3$:Ce (yttrium aluminum perovskite activated by cerium, or YAP:Ce) finger crystals (2×2×30 mm^3). The matrix is directly coupled to a 3-in. PS-PMT (Hamamatsu R2486-06). The modules are positioned on a rotating gantry, where opposing detectors are in time coincidence and can be set at a distance ranging from 10 to 25 cm so as to give the possibility of choosing the maximum spatial resolution (larger distance) or maximum sensitivity (smaller distance) configuration. The system operates in 3D data acquisition mode and an expectation maximization algorithm is used for image reconstruction [94], thus permitting the utilization of all the acquired data. The scanner has an axial field of view of 4 cm and a transaxial diameter of 4 cm, permitting both rat and mice studies. In PET mode, the spatial resolution is constant over the whole field of view and is better than 1.8 mm FWHM; the volume resolution at the center of the tomograph is 5.8 mm^3. The sensitivity at the center of the field of view is 17.3 cps/kBq (640 cps/μCi) with the detectors 15 cm apart. In SPET mode, the sensitivity is 114 cps/MBq and the spatial resolution is better than 3.5 mm FWHM.

The HIDAC-PET tomograph is based on a high density avalanche gas chamber (HIDAC) (Fig. 10c). The HIDACs are multiwire proportional gas chambers with the addition of a conversion/multiplication structure, made of a laminated plate containing interleaved lead and insulating sheets and drilled so as to form a dense honeycomb structure. The third generation of this scanner, called Quad-HIDAC, uses four detectors instead of two and has a larger detection solid angle. Each detector is made of eight chambers with increasing dimensions toward the exterior. The Quad-HIDAC scanner [95] has a field of view of 28 cm axially and 17 cm diameter, and exhibits a volume spatial resolution of 1.05 mm (transaxial) ×1.0 mm (axial) ×1.04 mm (tangent). The absolute sensitivity at the center of the field of view is 18 cps/kBq (666 cps/µCi).

Future directions in PET technology

Discussions on how to further improve PET performance have focused on the two parameters that most affect lesion detectability: sensitivity and resolution. In 2D PET acquisition mode, sensitivity can be improved by reducing the length of the septa, thereby increasing the acceptance angle of the detectors, but this gain in sensitivity is at the cost of a reduction in image resolution. The larger focus is on how to improve 3D acquisition. Here the principal hurdles are how to remove the increased scatter fraction and how to reduce random events. It is with the objective of overcoming these hurdles that scientists and engineers are interested in exploring the properties of alternative detector materials. The property that affects sensitivity is $\rho Z_{\mathrm{eff}}^{4}$, which for all current known detectors is highest for BGO. The search for new crystals is focusing on attempting to keep $\rho Z_{\mathrm{eff}}^{4}$ close to that of BGO, while improving on the properties where BGO is suboptimal. The property that affects the coincidence timing window is the lifetime of the fluorescent emission. The property that affects the accuracy in determining the position of an event within a detector block and also impacts on energy resolution is the light output that can be collected within the coincidence timing window. Higher light output can therefore improve spatial resolution and energy discrimination, thereby reducing the scatter fraction. It is for these reasons that commercial companies have invested in the development of LSO and GSO crystals for PET detector blocks.

A gain, which would have a potentially significant effect on PET, would be the ability to reduce the coincidence timing window by an order of magnitude. Such gains would require advances in photodetector technology and signal processing electronics. This would not only result in improvements in the NEC, through the reduction in randoms, but also provide the ability to perform time-of-flight PET reconstruction. With a timing resolution of <0.5 ns, it becomes possible to define the site of positron annihilation to within a line segment (<7.5 cm), and thereby to improve the reconstruction. A timing resolution of 0.05 ns would define positron annihilation to within 0.75 cm, and completely obviate the need for image reconstruction [78]. However, this value is still very far from being achieved.

Several advances in read-out electronics (dual photodetector readout) coupled with novel detector design (phoswich) promise great rewards in delivering improved and more uniform scanner resolution as DOI compensation becomes possible. Prototype detector modules have been constructed, with demonstration of the feasibility of DOI measurements, and these are perhaps the next major advance in clinical PET technology.

In parallel with detector module development, there are continual advances in image processing. For example, high-speed iterative reconstruction algorithms have resulted in substantial improvements in image quality on clinical scanners, especially at the interface between hot and cold structures. Improvements in scatter correction methods are continually evolving [14]. Monte Carlo methods to simulate the history of photon interactions within the patient and the scanner are under development (e.g., the International consortium OpenGate, www.opengate.org). This approach promises to provide the ability to account for numerous image-degrading effects: resolution recovery, scatter photons, and cascade gamma emission from complex PET tracers.

Reimbursement for PET examinations is likely to provide further impetus for the development of dedicated PET units with specialized functions: imaging of the brain, heart, and breast. Dedicated clinical PET brain scanners of reduced ring diameter are able to achieve spatial resolutions down to 2×2×2 mm^{3}, in contrast to whole-body instruments. It is in this arena where it is most likely that we shall see the first combined PET/MRI units, which are currently being explored for small animal imaging [96, 97]. Another area in which clinical prototype instruments have been built is dedicated PET mammography (PEM). These instruments overcome the weakness of whole-body scanners for breast imaging, with their inability to exploit the unique geometry of the breast. The specific design requirements for PEM systems exploit the ability to distend the breast away from the thorax as well as to compress it, thereby minimizing scatter and allowing the detectors to be placed in close proximity to the breast tissue. Designs analogous to conventional X-ray mammography, with breast compression, have been proposed [98, 99, 100, 101]; these consist of two parallel detector planes and also rectangular box detector configurations. Important demands on such a system are high sensitivity, due to time constraints on account of patient discomfort, and high resolution, approaching that of X-ray mammography.

Finally, PET/CT units customized for use by radiation oncologists are currently being developed by all of the major manufacturers. These PET/CT scanners consist of an expanded patient aperture (70-cm contiguous bore) that allows the patient to safely pass through the scanner in an immobilization cast, rigid indexing of the scanner image planes to an external laser triangulation system to identify the isocenter and field margins for tattoo placement, and specialized software for delineation of target volumes, beam's eye view projections, etc. The use of PET tracers in radiation treatment planning holds the promise of providing a radiobiological basis for IMRT dose painting from non-invasive images of tumor biology in addition to conventional CT anatomical considerations [102].

Acknowledgements. The authors would like to give special thanks to James Bland (CTI Knoxville, TN), Phil Vernon (General Electric, Toledo, OH), and Joel Karp (U.Penn, Philadephia, PA) for providing assistance in the preparation of Table 3, and to Bill Strauss (MSKCC, New York) for providing the impetus for this manuscript, for his excellent suggestions regarding content, and for his assistance in editing the final draft.

References

1. Phelps ME, Hoffman EJ, Mullani NA, Ter-Pogossian MM. Application of annihilation coincidence detection to transaxial reconstruction tomography. *J Nucl Med* 1975; 16:210–224.
2. Yamamoto Y, Thompson CJ, Diksic M, Meyer M, Feindel WH. Positron emission tomography. *J Radiat Phys Chem* 1984; 24:385–403.
3. Phelps ME, Mazziotta JC, Schelbert HR. *Positron emission tomography and autoradiography*. New York: Raven Press, 1986.
4. Budinger TF, Derenzo SE, Huesman RH, Cahoon JL. *PET: instrumentation perspectives*. Proceedings of the Society of Photo-optical Instrumentation Engineers 1982; 372:3–13.
5. Wahl RL, ed. *Principles and practice of positron emission tomography.* Philadelphia: Lippincott Wiliams & Wilkins, 2002.
6. Fermi E. *Nuclear physics*. Chicago: The University of Chicago Press, 1949.
7. Heitler W. *The quantum theory of radiation*. New York: Dover Publications, 1953.
8. Cho ZH, Chan JK, Ericksson L, Singh M, Graham S, MacDonald NS, Yano Y. Positron ranges obtained from biomedically important positron-emitting radionuclides. *J Nucl Med* 1975; 16:1174–1176.
9. Wu CS, Shaknov I. The angular correction of scattered annihilation radiation. *Phys Rev* 1950; 77:136.
10. Eisberg R, Resnick R. *Quantum physics of atoms, molecules, solids, nuclei, and particles.* New York: Wiley, 1985.
11. Brownell GL, Sweet WH. Localitation of brain tumours with positron emitters. *Nucleonics* 1953; 11:40–45.
12. Colombino P, Fiscella B, Trossi L. Study of positronium in water and ice from 22 to −144°C by annihilation quanta measurements. *Il Nuovo Cimento* 1965; xxxviii(2):707–723.
13. Berko S, Hereford FL. Experimental studies of positron interactions in solids and liquids. *Rev Modern Phys* 1956; 28:299–307.
14. Zaidi H. Comparative evaluation of scatter correction techniques in 3D positron emission tomography. *Eur J Nucl Med* 2000; 27:1813–1826.
15. Melcher CL. Scintillation crystals for PET. *J Nucl Med* 2000; 41:1051–1055.
16. Visser V, Melcher CL, Schweitzer JS, Suzuki H, Tombrello TA. Photo stimulated luminescence and thermoluminescence of LSO scintillators. *IEEE Trans Nucl Sci* 1994; 41:689–693.
17. Dorendos P, van Eijk CWE, eds. Proceedings int. conf. on inorganic scintillators and their applications, SCINT 95. Delft: Delft University Press, 1996.
18. Balcerzyk M, Moszynski M, Kapusta M, Szawlowski M. Timing properties of LuAP:Ce studies with large area avalanche photodiodes. *IEEE Trans Nucl Sci* 2001; NS-48: 2344–2347.
19. Moses WW, Weber MJ, Derenzo SE, Perry D, Berdahl P, Boatner LA. Prospects for dense infrared scintillators. *IEEE Trans Nucl Sci* 1998; 45:462–466.
20. Lerch MLF, Rosenfeld AB, Taylor GN, Meikle SR, Perevertailo VL. Spectral characterization of blue-enhanced silicon photodiode. *IEEE Trans Nucl Sci* 2001; 48:1220–1224.
21. Cherry SR, Shao Y, Tornai M, Siegel S, Ricci AR, Phelps ME. Collection of scintillation light from small BGO crystals. *IEEE Trans Nucl Sci* 1995; 42:1058–1063.
22. Adam LE, Karp JS, Daube-Witherspoon ME, Smith RJ. Performance of a whole-body PET scanner using curve-plate NaI(Tl) detectors. *J Nucl Med* 2001; 42:1821–1830.
23. Karp JS, Muehllehner G, MankofF DA, Ordonez CE, Ollinger JM, Daube-Witherspoon ME, Haigh AT, Beerbohm DJ. Continuous-slice PENN-PET: a positron tomograph with volume imaging capability. *J Nucl Med* 1990; 31:617–627.
24. Kapusta M, Moszynski M, Balcerzyk M, Braziewicz J, Wolski D, Pawelke J, Klamra W. Comparison of the scintillation properties of LSO:Ce manufactured by different laboratories and of LGSO:Ce. *IEEE Trans Nucl Sci* 2000; 47:1341–1345.
25. Casey ME, Erikson L, Schmand M, Andreaco MS, Paulus M, Dahlbom M, Nutt R. Investigation of LSO crystal for high spatial resolution positron emission tomography. IEEE Trans Nucl Sci 1997; 44:1109–1113.
26. Saoudi A, Pepin C, Pepin C, Houde D, Lecomte R. Scintillation light emission studies of LSO scintillators. *IEEE Trans Nucl Sci* 1999; 46:1925–1928.
27. Balcerzyk M, Moszynski M, Kapusta K, Wolski D, Pawelke J, Melcher CL. YSO, LSO, GSO and LGSO. A study of energy resolution and nonproportionality. *IEEE Trans Nucl Sci* 2000; 47:1319–1323.
28. Melcher CL, Schweitzer JS. Cerium-doped lutetium oxyorthosilicate: a fast and efficient new scintillator. *IEEE Trans Nucl Sci* 1992; NS-39:502–505.
29. Muehllehner G, Karp JS, Surti S. Design considerations for PET scanners. *Q J Nucl Med* 2002; 46:16–23.
30. Wojtowicz AJ, Szupryczynski P, Wisniewski D, Glodo J, Drozdowski W. Electron traps and scintillation mechanisms in $LuAlO_3$:Ce. *J Phys Condensed Matter* 2001; 13:9599–9619.
31. Moszynski M, Wolski D, Ludziejewski T, Kapusta M, Lempicki A, Brecher C, Wisniewski D, Wojtowicz AJ. Properties of the new LuAP:Ce scintillator. *Nucl Instrum Meth* 1997; A385:123–131.
32. Shlichta PJ. An exhaustive and systematic search for optimal PET scintillator materials. Presented at IEEE NSS and MIC Conference 2001, Conference Record, N12-69. *IEEE Trans Nucl Sci* 2002; NS-49.
33. DeRenzo SE, Weber MJ. Prospects of first-principle calculations of scintillator properties. *Nucl Instrum Meth* 1999; A422:111–118.
34. Lecoq P, Korzhik M. New inorganic scintillation materials development for medical imaging. *IEEE Trans Nucl Sci* 2002; 49:1651–1654.

35. Van Eijk CWE. Inorganic scintillators in medical imaging. *Phys Med Biol* 2002; 47:R85–R106.
36. Moses WW, Derenzo SE, Budinger TF. PET detector modules on novel detector technologies. *Nucl Instrum Meth* 1994; A353:189–194.
37. Knoll GF. *Radiation detection and measurement, 3rd edn.* New York: Wiley, 2000.
38. Sze SM. *Physics of semiconductor devices.* New York, Wiley, 1981.
39. Gatti E, Rehak P. Semiconductor drift chamber on application of novel charge transport scheme. *Nucl Instrum Meth* 1984; A225:608–614.
40. Lutz G. Semiconductor radiation detectors. *Nucl Instrum Meth* 1995; A367:21–33.
41. Delaney CFG, Finch EC. Some simple considerations on pulse shapes in radiation detectors. *Am J Phys* 1984; 52:351–354.
42. Radeka V. Low noise techniques in detectors. *Phys Rev Nucl Part Sci* 1988; 38:217–277.
43. Groom DE. Silicon photon diode detection of bismuth-germanate scintillator light. *Nucl Instrum Meth* 1984; A219:141–148.
44. Holland SE, et al. Development of low noise, back-side illuminated silicon photodiode array. *IEEE Trans Nucl Sci* 1997; NS-44:443–447.
45. Gruber GI, et al. A compact 64 pixel Cs(Tl)/Si PIN photodiode imaging module with IC readout. *IEEE Trans Nucl Sci* 2002; NS-49:147–152.
46. Levin CS, Hoffman EJ. Investigation of a new readout scheme for high resolution scintillation crystals arrays using photodiodes. *IEEE Trans Nucl Sci* 1997; NS-44:1208.
47. Moses WW, Derenzo SE. Gamma ray spectroscopy and timing using LSO and PIN photodiodes. *IEEE Trans Nucl Sci* 1995; NS-42:597.
48. Patt BE, Iwanczyk JS, Tull CR, Segal JD, MacDonald LR, Tornai MP, Kenney CJ, Hoffman EJ. Fast timing silicon photodetectors. *IEEE Trans Nucl Sci* 2000; 47:957–964.
49. Allier CP, Valk H, Huizenga J, Bom VR, Hollander RW, van Eijk CWE. Comparison study of silicon detectors. *IEEE Trans Nucl Sci* 1998; 45:576–580.
50. Lecomte R, Cadorette J, Richard P, Rodrigue S, Rouleau D. Design and engineering aspects of a high resolution positron for small animal imaging. *IEEE Trans Nucl Sci* 1994; 41:1446–1452.
51. Shah KS, Farrell R, Cirignano L, Grazioso R, Bennett P. Large-area APDs and monolithic APD arrays. *IEEE Trans Nucl Sci* 2001; NS-48:2352–2356.
52. Pichler B, Boning G, Lorenz E, Mirzoyan R, Pimpl W, Schwaiger M, Ziegler SI. Studies with a prototype high resolution PET scanner based on LSO-APD modules. *IEEE Trans Nucl Sci* 1998; 45:1298–1302.
53. Fazzi A Pignatel GU, Dalla Betta GF, Boscardin M, Varoli V, Verzellesi G. Charge preamplifier for hole collecting PIN diode and integrated tetrode N-JFET. *IEEE Trans Nucl Sci* 2000; 47:829–833.
54. Moses WW,.Derenzo SE, Nutt R, Digby WM, Williams CW, Andreaco M. Performance of PET detector module utilizing an array of silicon photodiodes to identify the crystal of interaction. *IEEE Trans Nucl Sci* 1993; 40:1036–1040.
55. Moses WW, Derenzo SE. Design studies for a PET detector module using a PIN photodiodes to measure depth of interaction. *IEEE Trans Nucl Sci* 1994; 41:1441–1445.
56. Huber JS, Moses WW, Virador PRG. Calibration of PET detector module that measure depth of interaction. *IEEE Trans Nucl Sci* 1998; 45:1268–1272.
57. Huber JS, Moses WW, Andreaco MS, Petterson O. An LSO scintillator array for a PET detector module with depth of interaction measurements. *IEEE Trans Nucl Sci* 2001; 48: 684–688.
58. Rogers JG Moisan C, Hoskinson EM, Andreaco MS, Williams CW, Nutt R. A practical block detector for a depth encoding PET camera. *IEEE Trans Nucl Sci* 1996; 43:3240–3248.
59. Robar JL, Thompson CJ, Murthy K, Clancy R, Bergman AM. Construction and calibration of detectors for high resolution metabolic breast cancer imaging. *Nucl Instrum Meth* 1997; 392:402–406.
60. Miyaoka RS, Lewellen TK, Yu H, McDaniel DL. A depth of interaction PET detector module. *J Nucl Med* 1998; 39:772 Suppl S.
61. Shao YP, Cherry SR, Siegel S, Silverman RW, Majewski S. Evaluation of multi-channel PMTs for readout of scintillator arrays. *Nucl Instrum Meth* 1997; A390:209–218.
62. Shao Y, Cherry SR. A study of depth of interaction measurements using bent optical fibers. *J Nucl Med* 1998; 39:191 Suppl S.
63. Yamamoto S, Ishibashi I, "A GSO depth of interaction detector for PET. *IEEE Trans Nucl Sci* 1998; 45:1078–1082.
64. Schmand M, Eriksson L, Casey ME, Wienhard K, Flugge G, Nutt R. Advantages using pulse shape discrimination to assign the depth of interaction information (DOI) from a multi layer phoswich detector. *IEEE Trans Nucl Sci* 1999; 46:985–990.
65. Inadama N, Murayama H, Omura T, Yamashita T, Yamamoto S, Ishibashi H, Kawai H, Omi K, Umehara T, Kasahara T. A depth of interaction detector for PET with GSO doped with different amount of CE. *IEEE Trans Nucl Sci* 2002; 49: 629–633.
66. Murayama H, Ishibashi H, Uchida H, Omura T, Yamashita T. Depth encoding multicrystal detector for PET. *IEEE Trans Nucl Sci* 1998; 45:1152–1157.
67. MacDonald LR, Dahlbohm M. Depth of interaction for PET using segmented crystals. *IEEE Trans Nucl Sci* 1998; 45: 2144–2148.
68. Shao Y, Silverman RW, Farrell R, Cirignano L, Grazioso R, Shah KS, Visser G, Clajus M, Tumer TO, Cherry SR. Design studies of a high resolution PET detector using APD arrays. *IEEE Trans Nucl Sci* 2000; 47:1051–1057.
69. Fremout AAR, Chen RR, Bruyndonckx P, Tavernier SPK. Spatial resolution and depth of interaction studies with a PET detector module composed of LSO and an APD array. *IEEE Trans Nucl Sci* 2002; 49:131–138.
70. Levin CS. Design of a high resolution and high sensitivity scintillation crystal array with nearly perfect light collection. *IEEE Trans Nucl Sci* 2002; 49:2236–2243.
71. Nutt R. The history of positron emission tomography. *Mol Imag Biol* 2002; 4:11–26.
72. Kops ER, Herzog H, Schmid A, Holte S, Feinendegen LE. Performance characteristics of an eight-ring whole body PET scanner. *J Comput Assist Tomogr* 1990; 14:437–445.
73. Senda M, Tamaki N, Yonekura Y, Tanada S, Murata K, Hayashi N, Fujita T, Saji H, Konishi J, Torizuka K. Performance characteristics of Positologica III: a whole-body positron emission tomograph. *J Comput Assist Tomogr* 1985; 9:940–946.
74. Wienhard K, Eriksson L, Grootoonk S, Casey M, Pietrzyk U, Heiss WD. Performance evaluation of the positron scanner ECAT EXACT. *J Comput Assist Tomogr* 1992; 16:804–813.
75. Wienhard K, Dahlbom M, Eriksson L, Michel C, Bruckbauer T, Pietrzyk U, Heiss WD. The ECAT EXACT HR: perfor-

mance of a new high resolution positron scanner. *J Comput Assist Tomogr* 1994; 18:110–118.

76. Mullani NA, Gould KL, Hartz RK, Hitchens RE, Wong WH, Bristow D, Adler S, Philippe EA, Bendriem B, Sanders M. Design and performance of POSICAM 6.5 BGO positron camera. *J Nucl Med* 1990; 5:628–631.
77. DeGrado TR, Turkington TG, Williams JJ, Stearns CW, Hoffman JM, Coleman RE. Performance characteristics of a whole-body PET scanner. *J Nucl Med* 1994; 35:1398–1406.
78. Moses WW. Time of flight in PET revisited. *IEEE Trans Nucl Sci* 2003: in press.
79. NEMA Standard Publication NU 2-1994. Performance measurements of positron emission tomographs. Washington: National Electrical Manufacturers Association, 1994.
80. NEMA Standard Publication NU 2-2001. Performance measurements of positron emission tomographs. Rosslyn, VA: National Electrical Manufacturers Association, 2001.
81. Daube-Witherspoon ME, Karp JS, Casey ME, DiFilippo FP, Hines H, Muehllehner G, Simcic V, Stearns CW, Adam LE, Kohlmyer S, Sossi V. PET performance measurements using the NEMA NU 2-2001 standard. *J Nucl Med* 2002; 43: 1398–1409.
82. Badawi RD, Marsden PK, Cronin BF, Sutcliffe JL, Maisey MN. Optimization of noise-equivalent count rates in 3D PET. *Phys Med Biol* 1996; 41:1755–1776.
83. Nehmeh SA, Erdi YE, Ling CC, Rosenzweig KE, Squire OD, Braban LE, Ford E, Sidhu K, Mageras GS, Larson SM, Humm JL. Effect of respiratory gating on reducing lung motion artifacts in PET imaging of lung cancer. *Med Phys* 2002; 3:366–371.
84. Kadrmas DJ, Christian PE. Comparative evaluation of lesion detectability for 6 PET imaging platforms using a highly reproducible whole-body phantom with (22)Na lesions and localization ROC analysis. *J Nucl Med* 2002; 43:1545–1554.
85. Paigen K. A miracle enough: the power of mice. *Nature Med* 1995; 1:215–220.
86. Chien KR. Genes and physiology: molecular physiology in genetically engineered animals. *J Clin Investig* 1996; 97:901–909.
87. Phelps ME. PET: the merging of biology and imaging into molecular imaging. *J Nucl Med* 2000; 41:661–681.
88. Cutler PD, Cherry SR, Hoffman EJ. Design features performance of a PET system for animal research. *J Nucl Med* 1992; 33:595–604.
89. Hichwa R. Are animal scanners really necessary for PET? *J Nucl Med* 1994; 35:1396–1397.
90. Del Guerra A, Belcari N. Advances in animal PET scanners. *Q J Nucl Med* 2002; 46:35–47.
91. Chatziioannou AF, Cherry SR, Shao Y, Silverman RW, Meadors K, Farquhar TH, Pedarsani M, Phelps ME. Performance evaluation of microPET: a high-resolution lutetium oxyorthosilicate PET scanner for animal imaging. *J Nucl Med* 1999; 40:1164–1175.
92. Chatziioannou A, Tai YC, Doshi N, Cherry SR. Detector development for microPET II: a 1 microl resolution PET scanner for small animal imaging. *Phys Med Biol* 2001; 46: 2899–2910.
93. Del Guerra A, Di Domenico G, Scandola M, Zavattini G. YAP-PET: first results of a small animal positron emission tomograph based on YAP:Ce finger crystals. *IEEE Trans Nucl Sci* 1998; 45:3105–3108.
94. Motta A, Damiani C, Del Guerra A, Di Domenico G, Zavattini G. Use of a fast deconvolution EM algorithm for 3-D image reconstruction with the YAP-PET tomograph. *Computerized Medical Imaging and Graphics* 2002; 26:293–302.
95. Jeavons AP, Chandler RA, Dettmar CAR. A 3D HIDAC-PET camera with sub-millimetre resolution. *IEEE Trans Nucl Sci* 1999; 46:468–473.
96. Slates RB, Farahani K, Shao Y, Marsden PK, Taylor J, Summers PE, Williams S, Beech J, Cherry SR. A study of artefacts in simultaneous PET and MR imaging using a prototype MR compatible PET scanner. *Phys Med Biol* 1999; 44: 2015–2027.
97. Jakobs RE, Cherry SR. Complementary emerging techniques: high-resolution PET and MRI. *Curr Opin Neurobiol* 2001; 11:621–629.
98. Moses WW, Qi J. Fundamental limits of positron emission mammography. *Nucl Instrum Meth* 2003; A497A:82–89.
99. Thompson CJ, Murthy K, Weinberg IN, Mako R. Positron emission mammography (PEM): a promising technique for detecting breast cancer. *IEEE Trans Nucl Sci* 1995; 42: 1012–1017.
100. Raylman RR, Majewski S, Wojcik R, Weisenberger AG, Kross B, Popov V, Bishop HA. The potential role of positron emission mammography for detection of breast cancer. A phantom study. *Med Phys* 2000; 27:1943–1954.
101. Del Guerra A, Belcari N, Bencivelli W, Motta A, Righi S, Vaiano A, Di Domenico G, Moretti E, Sabba N, Zavattini G, Campanini R, Lanconelli R, Riccardi A, Cinti MN, Pani R. Monte Carlo study and experimental measurements of breast tumor detectability with a novel PEM apparatus. Conference Records of the 2002 IEEE Nuclear Science Symposium and Medical Imaging Conference, Norfolk, Virginia, USA, 10–16 November 2002, and submitted to *IEEE Trans Nucl Sci* 2003: in press.
102. Ling CC, Humm JL, Larson SM, Amols H, Fuks Z, Leibel S, Koutcher JA. Towards multidimensional radiotherapy (MD-CRT): biological imaging and biological conformality. *Int J Radiat Oncol Biol Phys* 2000; 47:551–560.